

Grant Agreement N°763990

## UPWARDS

### Deliverable D5.1

#### 3D progressive fatigue delamination model

<b>WP</b>	5	Material failure models
<b>Task</b>	5.1	3D progressive delamination method based on cohesive zone modelling for fatigue loading

<b>Dissemination level</b> <sup>1</sup>	PU	<b>Due delivery date</b>	30/11/2020 (31/03/2020)
<b>Nature</b> <sup>2</sup>	R	<b>Actual delivery date</b>	12/02/2021

<b>Lead beneficiary</b>	Aalborg University
<b>Contributing beneficiaries</b>	SAMTECH SA, Siemens Gamesa Renewable Energy SA

Document Version	Date	Author	Comments
1	19/01/2021	Laura Carreras (AAU), Brian Bak (AAU), Esben Lindgaard (AAU), Cédric Lequesne (SAMCEF), Hu Xiong (SAMCEF)	Creation

<sup>1</sup> Dissemination level: **PU** = Public, **PP** = Restricted to other programme participants (including the JU), **RE** = Restricted to a group specified by the consortium (including the JU), **CO** = Confidential, only for members of the consortium (including the JU)

<sup>2</sup> Nature of the deliverable: **R** = Report, **P** = Prototype, **D** = Demonstrator, **O** = Other

<sup>3</sup> Creation, modification, final version for evaluation, revised version following evaluation, final

## Deliverable abstract

Long fibre-reinforced composite materials are especially suitable for wind turbine blades structural applications due to their outstanding specific mechanical properties compared to metallic alloys. However, composite elements are very sensitive to manufacturing defects and matrix micro-cracking that can lead to interply delamination and, thus, compromise the structural integrity. Adopting effective and accurate numerical tools able to predict the effects of damage on the carrying load capability of the structure reduces design, certification and maintenance costs. To this end, a fatigue-driven delamination method applicable to the 3D simulation of wind turbine blades is developed. The publications of the method in a scientific paper in a peer-reviewed international journal<sup>1</sup> and in the open access archive arXiv<sup>2</sup> are outcomes of this sub-task. The method is implemented in the SAMCEF commercial finite element code. A characterization testing campaign on coupon specimens dedicated to obtain the material properties to input the method is carried out. A batch of specimens made of a non-crimp fabric laminated glass fiber reinforced polymers (GFRP) used in SGRE wind turbine blades are tested for each material property. The model is validated by comparing simulated and testing results for a demonstrator specimen with curved delamination front that is selected to be more representative of structures in service. The implemented modelling framework is able to reproduce the experimental results on the demonstrator specimen in terms of crack front shape evolution and crack front location versus number of fatigue cycles with reasonable accuracy. Differences between both results show that the simulation is delayed with respect to the experimental results. However, these differences are deemed to fall within an acceptable range and might be attributed to the high dispersion in the results from coupon specimen used to characterize the fatigue properties of the interface. In any case, the order of magnitude of both result sources is comparable. The simulation tool sets the basis for a powerful tool for fatigue life prediction of laminated composite structure.

## Deliverable Review

Reviewer #1: /Coordinator				Reviewer #2:		
Answer	Comments	Type*	Answer	Comments	Type*	
1. Is the deliverable in accordance with						
(i) The Description of Work?	<input checked="" type="checkbox"/> Yes <input type="checkbox"/> No	<input type="checkbox"/> M <input type="checkbox"/> m <input type="checkbox"/> a	<input type="checkbox"/> Yes <input type="checkbox"/> No		<input type="checkbox"/> M <input type="checkbox"/> m <input type="checkbox"/> a	
(ii) The international State of the Art?	<input type="checkbox"/> Yes <input type="checkbox"/> No	<i>Not applicable for this deliverable</i>	<input type="checkbox"/> Yes <input type="checkbox"/> No	<i>Not applicable for this deliverable</i>	<input type="checkbox"/> M <input type="checkbox"/> m <input type="checkbox"/> a	
2. Is the quality of the deliverable in a status						
(i) That allows it to be sent to European Commission?	<input checked="" type="checkbox"/> Yes <input type="checkbox"/> No	<input type="checkbox"/> M <input type="checkbox"/> m <input type="checkbox"/> a	<input type="checkbox"/> Yes <input type="checkbox"/> No		<input type="checkbox"/> M <input type="checkbox"/> m <input type="checkbox"/> a	
(ii) That needs improvement of the writing by the originator of the deliverable?	<input type="checkbox"/> Yes <input checked="" type="checkbox"/> No	<input type="checkbox"/> M <input type="checkbox"/> m <input type="checkbox"/> a	<input type="checkbox"/> Yes <input type="checkbox"/> No		<input type="checkbox"/> M <input type="checkbox"/> m <input type="checkbox"/> a	
(iii) That needs further work by the Partners responsible for the deliverable?	<input type="checkbox"/> Yes <input checked="" type="checkbox"/> No	<input type="checkbox"/> M <input type="checkbox"/> m <input type="checkbox"/> a	<input type="checkbox"/> Yes <input type="checkbox"/> No		<input type="checkbox"/> M <input type="checkbox"/> m <input type="checkbox"/> a	

\* Type of comments: M = Major comment; m = minor comment; a = advice

## Table of Contents

---

<b>1. Introduction.....</b>	<b>4</b>
1.1. Background .....	6
1.2. Objectives.....	7
<b>2. Theoretical framework.....</b>	<b>8</b>
2.1. Cohesive zone model .....	8
2.2. Quasi-static loading .....	10
2.2.1. Propagation criterion .....	10
2.2.2. Onset criterion .....	11
2.2.3. Mode-mixity .....	11
2.3. Fatigue loading.....	12
2.3.1. Envelope load approach, damage rate and crack growth rate.....	12
2.3.2. Fatigue damage model.....	13
2.4. Arbitrarily shaped delamination fronts .....	14
2.4.1. Growth driving direction .....	15
2.4.2. J-integral .....	16
<b>3. Methodology .....</b>	<b>18</b>
3.1. Mechanical testing.....	18
3.1.1. Characterization of material properties .....	18
3.1.2. Testing of delamination demonstrator .....	25
3.2. Numerical modelling.....	29
3.2.1. Finite element model implementation in SAMCEF .....	29
3.2.2. Validation test case.....	33
3.2.3. Delamination demonstrator .....	36
<b>4. Results and discussion .....</b>	<b>38</b>
4.1. Characterization testing.....	38
4.1.1. Quasi-static properties .....	38
4.1.2. Fatigue properties .....	39
4.2. Delamination demonstrator – A comparison between testing and simulation results .....	41
4.2.1 Testing results of the delamination demonstrator.....	41
4.2.2 Simulation results of the implementation validation cases.....	44
4.2.3 DCB Fatigue test .....	47
4.2.4 Comparison of results on the demonstrator specimen .....	50
<b>5. Conclusions.....</b>	<b>59</b>
<b>6. References .....</b>	<b>60</b>

## 1. Introduction

Failure in laminated composites is usually caused by inter-laminar fractures, such as delamination or adhesive joint debonding, promoted by or coexisting with intra-laminar damage mechanisms, like matrix cracking and fiber failure (see Figure 1-1).

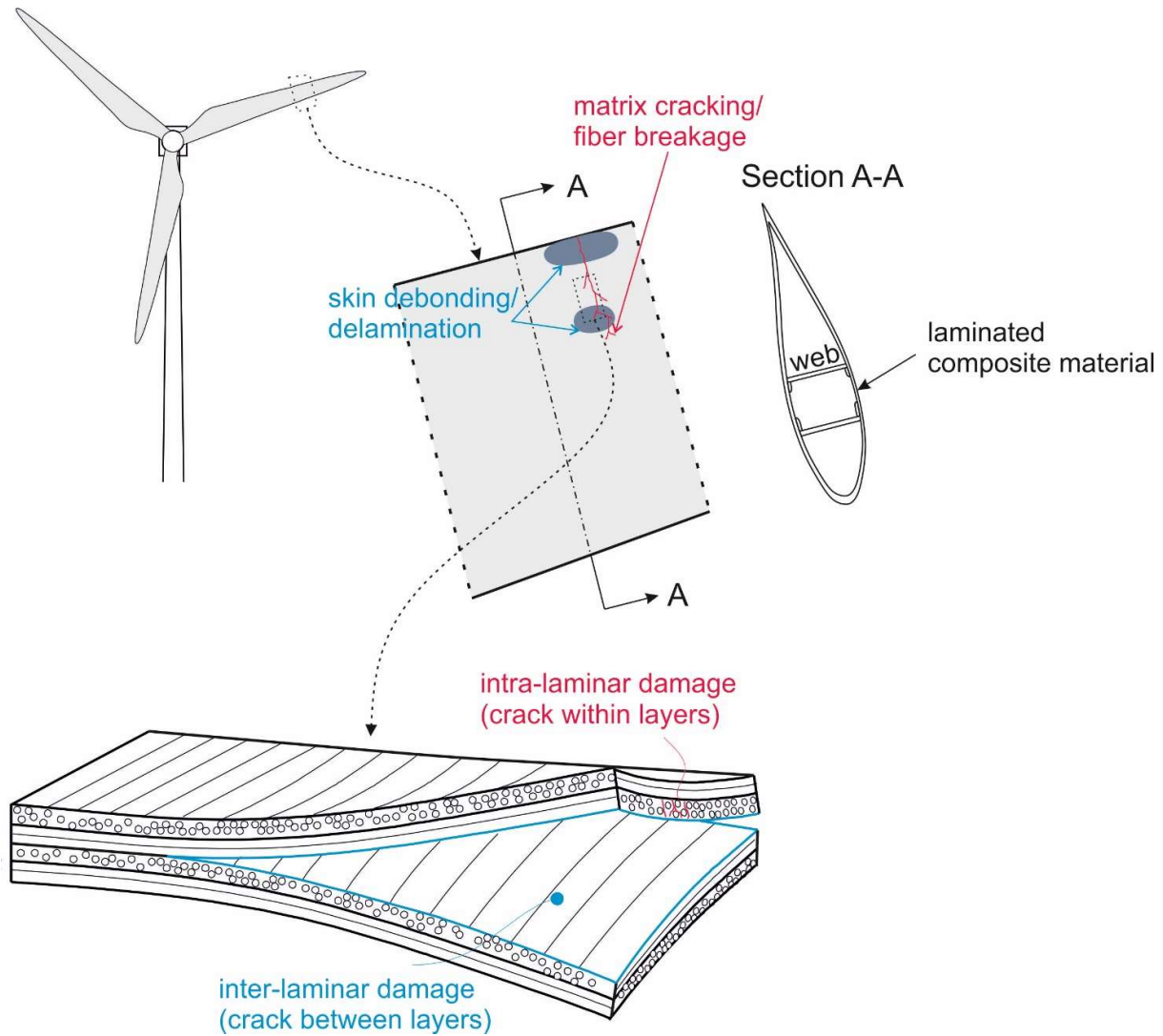


**Figure 1-1. Inter-laminar and intra-laminar damage in wind turbine blades made of a laminated composite material.**

Fatigue failure prediction, despite of being crucial for an accurate assessment of the service life of composite structures and a good planning of maintained actions, remains far from mature. The interaction between different failure mechanisms and the complexity of realistic loading spectra, spanning with varying amplitude and frequency, is currently not possible to predict with the state-of-the-art material damage models. The objectives of WP5 are the development of (i) progressive material damage models for both inter- and intra-laminar fracture and (ii) simulation tools for static and fatigue-driven damage development in laminated composite wind turbine blades in order to evaluate the structural performance and integrity.

First, independent inter- (T5.1) and intra-laminar (T5.2) fatigue damage models are developed. Then, a unified numerical framework is implemented in SAMCEF, including interaction between both models (T5.3). Then, the effect of fatigue loading history on damage development is studied and incorporated to the numerical tool (T5.4). Finally, the method is validated against experimental

testing on a wind turbine (WT) blade substructure (T5.5). The described workflow is illustrated in Figure 1-2.

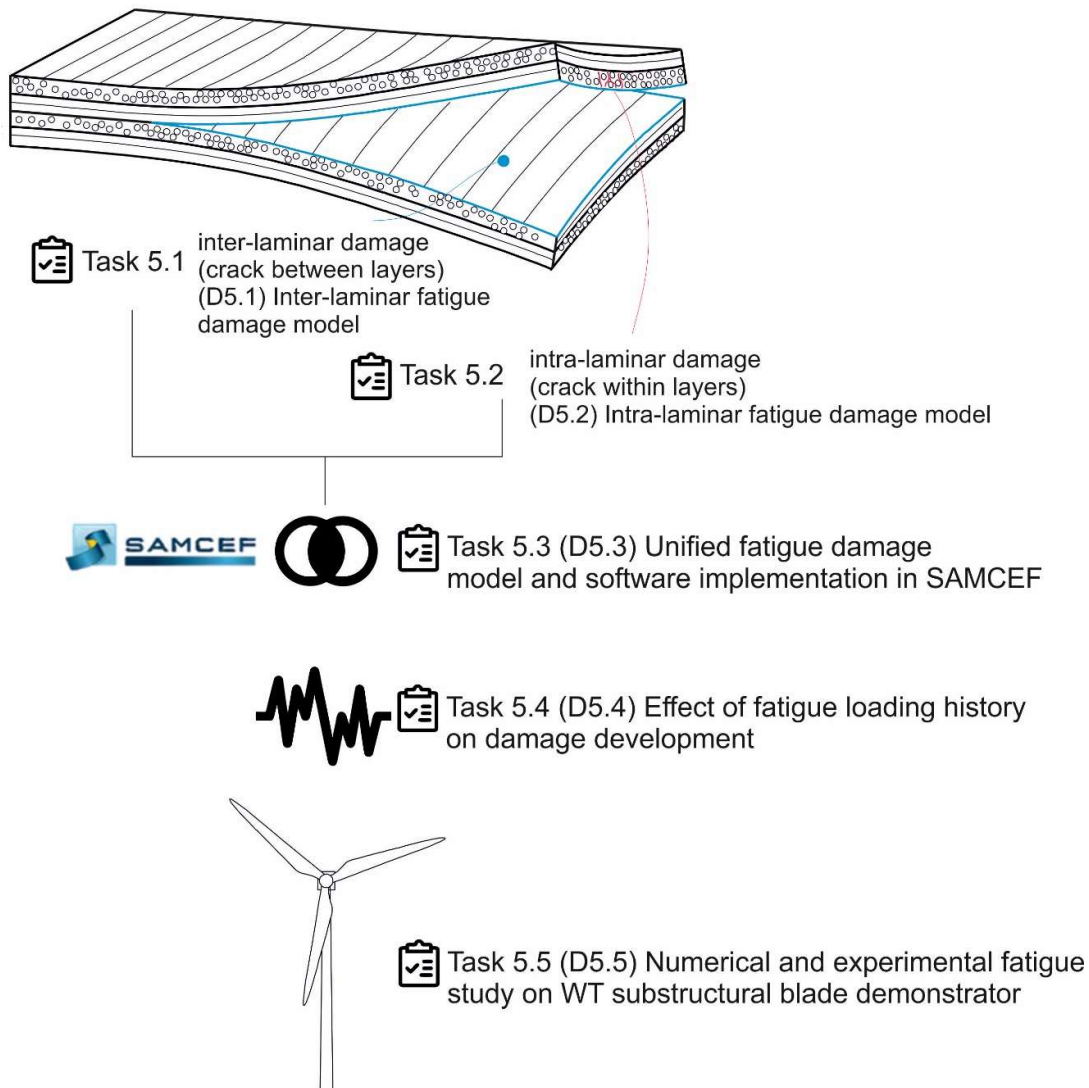


**Figure 1-2. Overview of tasks in work package WP5.**

This document describes the work carried out in Task 5.1. First, a 3D progressive delamination (inter-laminar damage) method based on cohesive zone modelling for fatigue loading was developed. This method was published in References<sup>1,2</sup> acknowledging the funding received from the UPWARDS project. The necessary material properties to input the model for both quasi-static and fatigue loading simulations were identified. A characterization testing campaign was designed and coupon test specimens were tested according to it. The method was implemented in SAMCEF and it is currently ready to use. The predictive capabilities of the simulation method were demonstrated on a delamination demonstrator by comparing numerical results to testing data. More precisely, the delamination front shape and location as a function of the testing time (or number of fatigue cycles) was compared. The method only uses the material properties, characterized using coupon specimens, to predict the fatigue behaviour of a demonstrator specimen with curved delamination front propagating under fatigue loading. The described workflow of Task 5.1 is illustrated in Figure 1-3.

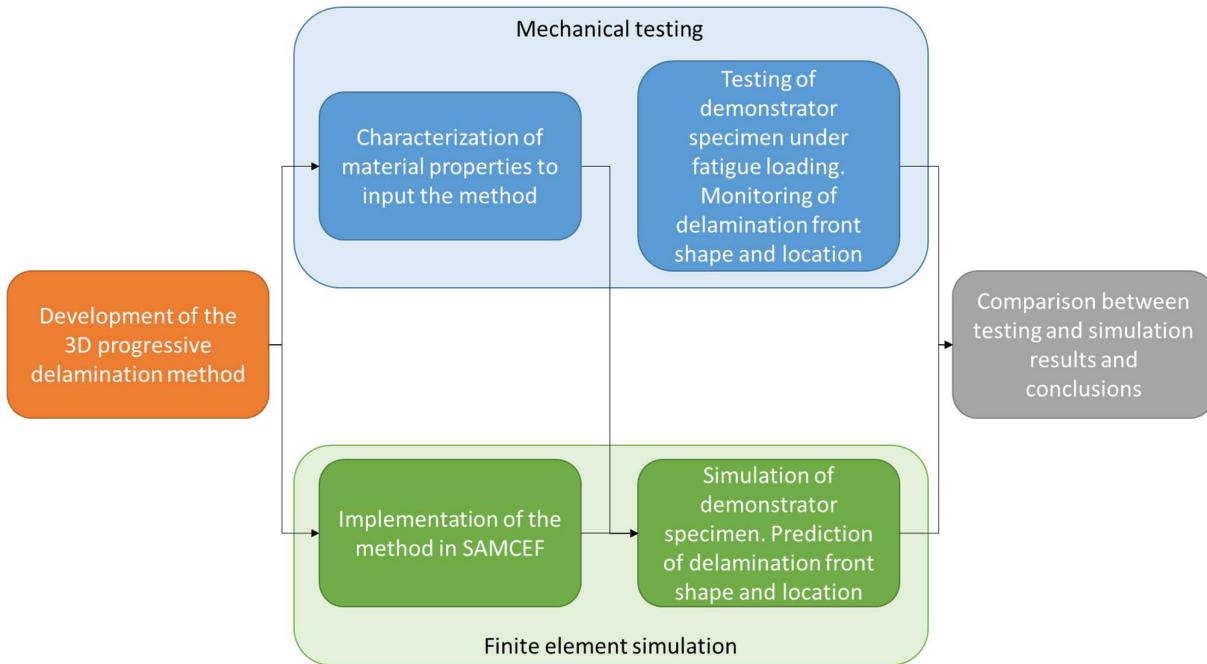


**Figure 1-3. Workflow in Task 5.1.**

This deliverable D5.1 is structured as follows: In Section 1.1, the background and what this study proposes to accomplish is described. In Section 1.2, the specific objectives of this deliverable are outlined. In Section 2, the main theoretical concepts related to the 3D progressive delamination method are presented. In Section 3.1, the methodology followed to test the coupon specimens to get the material properties and the demonstrator specimen to validate the model is described. In Section 3.2, the implementation of the method in SAMCEF and the procedure followed to carry out the simulation of the demonstrator specimen are detailed. In Section 4, the material properties obtained from the characterization testing campaign, as well as the comparison between testing and simulation results for the demonstrator specimen are presented. Finally, in Section 5, the main conclusions of this work are highlighted.

## 1.1. Background

Multiple models exist in the literature to deal with fatigue-driven delamination. However, although they succeed in reproducing the fatigue behavior at coupon level, most of them are not applicable or have not been validated for simulating larger structures. Thus, there is a need for efficient and reliable technologies, and design methodologies to account for delamination in complex layered composite structures under fatigue loading. On the one hand, these methodologies are needed for a proper dimensioning of the components (thus reducing the number of manufactured specimens needed for a trial and error optimization) and, on the other hand, to be able to anticipate the mechanical response to different infringed damage forms.

The most common methods for the prediction of inter-laminar failure can be divided into two main approaches: i) methods purely based on fracture mechanics and ii) methods based on the cohesive zone model (CZM) concept<sup>3,4</sup>, the latter combining the framework of fracture mechanics and damage mechanics. However, only CZMs can capture fracture energy dissipation mechanisms taking place at the fracture process zone, such as the formation of a fibre bridging zone ahead of the crack tip before complete separation of the crack faces. Therefore, the CZM approach is a suitable means of predicting delamination propagation when a non-negligible fracture process zone is present.

From a review of the methods based on the CZM approach available in the literature, it is detected that most of them are either limited to two dimensional (2D) applications or they have not been fully validated in three dimensional (3D) problems. In order to extend the general applicability of the existing methods, both new analysis techniques and experimental data of 3D delamination

propagation are needed. The point of departure of this task will be a recent 2D delamination fatigue model developed at AAU<sup>5</sup>. In this case, an efficient identification of the crack propagation direction and an accurate means of calculating the energy release rate in three-dimensional structures are needed for its 3D extension.

## **1.2. Objectives**

The overall objectives of Task 5.1 are:

- To investigate the existing simulation CZM methods for fatigue-driven delamination, with special attention to their 3D capabilities.
- To develop a new methodology to simulate fatigue-driven delamination based on the 2D delamination fatigue model developed at AAU<sup>5</sup> and implement it into the SAMCEF commercial finite element framework.
- To devise an experimental methodology to obtain the material card that feeds the simulation method.
- To validate the proposed methodology by comparing computational and experimental tests of a demonstrator representative of arbitrarily shaped delamination growth in a real structural component.

## 2. Theoretical framework

### 2.1. Cohesive zone model

At the macroscopic level, a delamination is analyzed as a single crack growing in a plane between layers. However, the mechanical behavior attributed to this failure mode is, in fact, the consequence of multiple failure events occurring at the microscopic level (matrix micro-cracking, void formation, non-linear material deformations, fibre-bridging, etc.). The concept of Cohesive Zone Model (CZM) accounts for the presence of a Fracture Process Zone (FPZ), called the cohesive zone, where all these microscopic events take place. The main assumption is that all the material deformation and degradation of the mechanical properties due to these failure processes can be lumped into a surface (the interface between plies).

The interfacial constitutive behavior is described in terms of the separation between the two initially coincident surfaces bounding the plies and the associated cohesive tractions that act to tie the surfaces together. The process of fracture initiates when the traction at the crack tip reaches the interfacial strength,  $\tau_o$ , which is the maximum traction that the interface can withstand. When the material cannot withstand any traction, the amount of energy dissipated per unit of newly created crack is equal to the fracture toughness (area under the traction-separation law),  $\mathcal{G}_c$  (see Figure 2-1). The softening function is considered a material property and can be derived experimentally<sup>6</sup>.

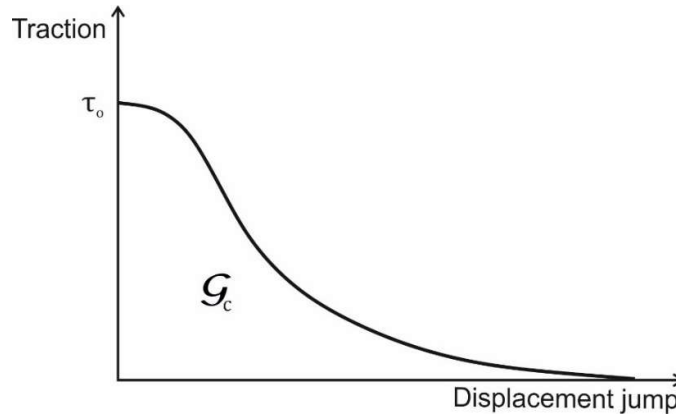
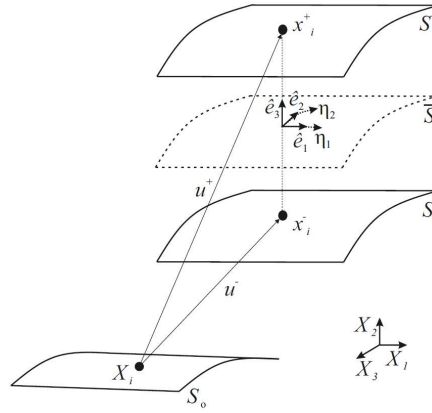


Figure 2-1. Cohesive law.

Different interpretations can be made of the physical processes underlying at the micro-scale that may determine the shape of the cohesive law. For instance, the presence of fibers bridging both fracture surfaces is a common phenomenon<sup>7</sup>, especially in higher mode I loading contributions. Fiber bridging, and subsequent fiber pull out and breakage, increases with crack length and its contribution is more important in unidirectional laminates<sup>8</sup>, even though it might also occur in other configurations<sup>9</sup>.

In the FE implementation, the cohesive behavior is reduced to the mid-surface  $\bar{S}$  between the upper surface,  $S^+$ , and the lower surface,  $S^-$  (see Figure 2-2). Thus, the deformed mid-surface is defined as the average distance between the two initially coincident delamination surfaces. The cohesive variables are calculated at the integration points, located on the mid-surface, and decomposed into mode I component (following the normal  $\vec{e}_3$ -direction to the midsurface) and shear components (following two tangential  $\vec{e}_1$  and  $\vec{e}_2$ -directions to the mid-surface).





**Figure 2-2. Description of the deformed element midsurface,  $\bar{S}^{10}$ .**

To address the process of fracture under changing mixed-mode conditions, an equivalent mixed-mode cohesive law in one dimension is formulated (see Figure 2-3).

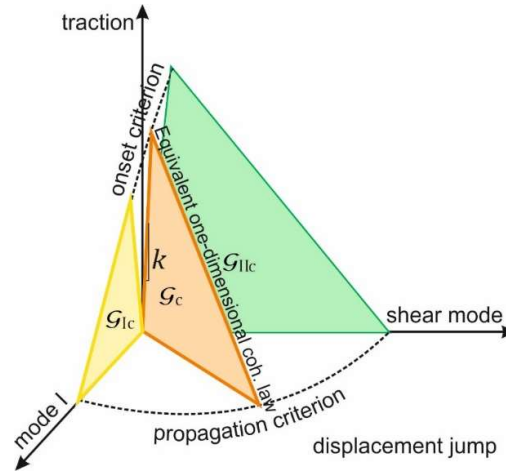


**Figure 2-3. Equivalent one-dimensional cohesive law.**

The CZM is formulated in the framework of damage mechanics to ensure irreversible crack propagation. By making use of a damage variable the restoration of the previous cohesive state between the interfacial surfaces is prevented. A thermodynamical interpretation of the irreversible process of fracture can be established by definition of an energy-based damage variable ( $\mathcal{D}^e$ ) as the fraction of dissipated specific energy ( $\omega_d$ ) to the energy necessary to create a unit of new surface ( $G_c$ ), see Figure 2-4. Thus,  $\mathcal{D}^e$  is related to the development of micromechanical failure processes and evolves monotonically with time.

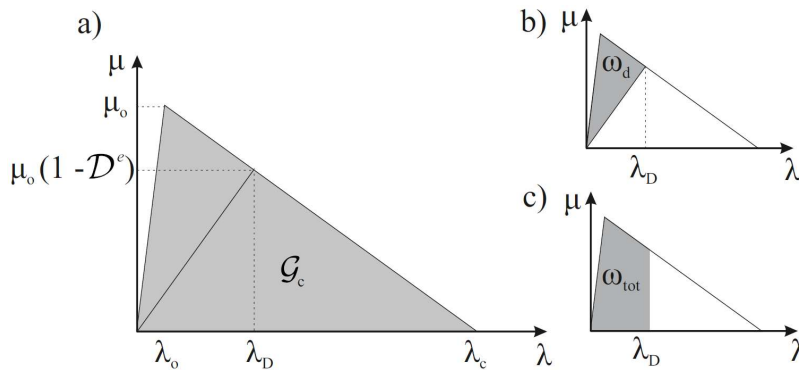


**Figure 2-4. Equivalent one-dimensional cohesive law. The shadowed area in a) represents the fracture toughness ( $G_c$ ); in b), the specific dissipated energy ( $\omega_d$ ); and in c), the total specific work ( $\omega_{tot}$ ) for a given state of damage<sup>11</sup>.**

Because the cohesive interface is zero-thickness, all deformations are assumed to be separation between ply surfaces. In order to avoid elastic opening of the cohesive interface, the initial stiffness should be infinite (i.e. the cohesive law starting without any separation until the interfacial strength,  $\tau_o$ , is reached). However, infinite stiffness must be avoided in the numerical implementation of the model into finite elements. Therefore, an elastic region is introduced before the initiation of the degradation process. This elastic region is defined by a penalty stiffness,  $k$  (see Figure 2-3). A stiffness degrading damage variable ( $\mathcal{D}^k$ ) is defined to ensure the irreversibility of the softening process. Thus,  $\mathcal{D}^k$  acts to degrade the interfacial stiffness:

$$\mu = (1 - \mathcal{D}^k) k \lambda \quad \text{Eq. 2-1}$$

For the formulation of the equivalent one-dimensional cohesive law, and so that different stages of the degrading process can be compared under changing mixed-mode loading conditions, a non-negative scalar displacement jump is defined:

$$\lambda = \sqrt{(\delta_I)^2 + (\delta_{sh})^2} \quad \text{Eq. 2-2}$$

where  $\delta_I$  is the mode I displacement jump, associated to the displacement jump in the normal direction to the mid-surface ( $\vec{e}_3$ ), and  $\delta_{sh}$  is the shear displacement jump resultant of the displacement jumps in the tangential directions to the mid-surface ( $\vec{e}_1$  and  $\vec{e}_2$ ):

$$\delta_I = \langle \delta_3 \rangle \quad \text{Eq. 2-3}$$

$$\delta_{sh} = \sqrt{(\delta_1)^2 + (\delta_2)^2} \quad \text{Eq. 2-4}$$

$\mu$  is the equivalent one-dimensional cohesive traction. Both damage variables ( $\mathcal{D}^e$  and  $\mathcal{D}^k$ ) are equivalent and uniquely related for a given state of damage.

The relation between the stiffness degrading damage variable and the equivalent one-dimensional displacement jump ( $\lambda$ ) reads:

$$\mathcal{D}^k = \frac{\lambda_c(\lambda - \lambda_o)}{\lambda(\lambda_c - \lambda_o)} \quad \text{Eq. 2-5}$$

And the energy-based damage variable is related to  $\mathcal{D}^k$  and  $\lambda$  as:

$$\mathcal{D}^e = 1 - \frac{\lambda_c(1 - \mathcal{D}^k)K\lambda}{2\mathcal{G}_c} \quad \text{Eq. 2-6}$$

## 2.2. Quasi-static loading

### 2.2.1. Propagation criterion

The fracture toughness ( $\mathcal{G}_c$ ) is the total amount of energy dissipated due to the combination of several fracture phenomena occurring at the microscale under stable and quasi-static propagation conditions. Since the acting failure mechanisms are different for every loading mode condition,  $\mathcal{G}_c$  is mode-dependent. This implies that the propagation criterion needs to be formulated in terms of the pure mode fracture toughnesses and the mixed mode ratio. The interaction between loading modes is done using the B-K criterion<sup>12</sup>:

$$\mathcal{G}_c = \mathcal{G}_{Ic} + (\mathcal{G}_{shc} - \mathcal{G}_{Ic})(B_{mm})^\eta \quad \text{Eq. 2-7}$$

where  $\mathcal{G}_{Ic}$  is the mode I fracture toughness,  $\mathcal{G}_{shc}$  the fracture toughness under shear loading,  $\eta$  is the B-K interaction parameter and  $B_{mm}$  is a measure of the mixed-mode ratio (see Section 2.2.3). Note that, since mode III fracture toughness is often higher than that of mode II loading, as a conservative approach, the fracture properties of mode II are generally attributed to any combination of shear mode. Thus,  $\mathcal{G}_{shc}$  is usually assumed equal to  $\mathcal{G}_{IIc}$ .

### 2.2.2. Onset criterion

In a general 3D case, the resultant traction at the cohesive surfaces is a combination of a normal (mode I) and two tangential components (shear modes). Thus, the onset criterion also needs to be interpolated through the different loading modes (see Figure 2-3). In this model, the propagation and initiation criteria are linked, such that the criterion for delamination onset is also based on the B-K criterion<sup>13</sup>:

$$(\mu_o)^2 = (\tau_{Io})^2 + ((\tau_{sh o})^2 - (\tau_{Io})^2)(B_{mm})^\eta \quad \text{Eq. 2-8}$$

where  $\mu_o$  is the equivalent one-dimensional interlaminar strength,  $\tau_{Io}$  is the mode I interlaminar strength and  $\tau_{sh o}$  is the shear mode interlaminar strength. Since it is assumed that the penalty stiffness ( $k$ ) is mode independent<sup>14</sup>, the relation between cohesive properties must fulfil:

$$\frac{\tau_{sh o}}{\tau_{Io}} = \sqrt{\frac{G_{sh c}}{G_{Ic}}} \quad \text{Eq. 2-9}$$

### 2.2.3. Mode-mixity

The fracture toughness under a combination of mixed-mode is usually reduced from tests, such as the mixed-mode (I+II) bending, assuming that the mixed-mode ratio during propagation is constant. In other words, the measured fracture toughness is related to a single global mixed-mode ratio. However, the mixed-mode ratio defined as the mode II component,  $G_{II}$ , over the total energy release rate,  $G_I + G_{II}$ , is not constant along the FPZ<sup>15</sup>. It is observed that the onset is mode II-dominated, while there is a higher mode I-contribution close to the completely damaged zone.

From a numerical point of view, the evaluation of the mixed-mode ratio using cohesive elements is typically done independently at each integration point. Local measurements of the work done by each component of cohesive traction and separation are used to compute the mode-decomposed  $G$ . In this way, the local mixed-mode ratio is computed as:

$$B_{mm} = \frac{\omega_{tot sh}}{\omega_{tot I} + \omega_{tot sh}} \quad \text{Eq. 2-10}$$

where  $\omega_{tot I}$  is the computed work done by the normal components of the cohesive traction and separation ( $\vec{e}_3$ -direction in Figure 2-2); and  $\omega_{tot sh}$  is the total computed work done by the shear components of the cohesive traction and separation ( $\vec{e}_1$ - and  $\vec{e}_2$ -directions in Figure 2-2):

$$\omega_{tot sh} = \omega_{tot 1} + \omega_{tot 2} \quad \text{Eq. 2-11}$$

It is worth noting that the implementation of the formulation in a cohesive element does not discriminate between the mode II and mode III components. Thus the two shear components,  $\omega_{tot 1}$  and  $\omega_{tot 2}$ , are not necessarily equivalent to the mode II and mode III components,  $\omega_{tot II}$  and  $\omega_{tot III}$ . See Figure 2-4-c) for an schematic representation of the total specific work  $\omega_{tot}$ .

Conversely, a global measure of the mode-mixity is defined as:

$$\Phi = \frac{G_{sh}}{G_I + G_{sh}} \quad \text{Eq. 2-12}$$

where  $G_I$  and  $G_{sh}$  are the energy release rates associated to mode I and shear loading. In this model, the evaluation of the energy release rates is made by means of the  $J$ -integral approach, which is able to decompose into modes II and III (see Section 2.4.2).

## 2.3. Fatigue loading

### 2.3.1. Envelope load approach, damage rate and crack growth rate

Real structures in service conditions are subjected to a complex, and in some cases, random sequence of loads of different amplitude. The loading spectrum introduces complexity in the modeling of the fatigue behavior. Thus, there exist several cyclic-counting algorithms (commonly called rain-flow algorithms<sup>16,17</sup> for reducing a spectrum of varying loading to a load cycle histogram. Once the spectrum is reduced into blocks of constant loading, the envelope load models, which only model the maximum cyclic load, are the most computationally efficient for high-cycle fatigue applications.

In this envelope load CZ method, the number of cycles is discretized and the damage variable,  $\mathcal{D}^e$ , is updated for each equilibrium step. The damage at a given number of cycles is determined by integration of the damage rate ( $d\mathcal{D}^e/dN$ ). The damage rate is linked to the crack growth rate ( $da/dN$ ) as:

$$\frac{d\mathcal{D}^e}{dN} = \frac{\partial \mathcal{D}^e(B_{mm}, \lambda)}{\partial a} \frac{da}{dN} = \left( \frac{\partial \mathcal{D}^e}{\partial B_{mm}} \frac{\partial B_{mm}}{\partial a} + \frac{\partial \mathcal{D}^e}{\partial \lambda} \frac{\partial \lambda}{\partial a} \right) \frac{da}{dN} \quad \text{Eq. 2-13}$$

where the partial derivatives  $\frac{\partial \mathcal{D}^e}{\partial B_{mm}}$  and  $\frac{\partial \mathcal{D}^e}{\partial \lambda}$  depend on the quasi-static cohesive zone model formulation and the current displacement field. These derivatives are further developed in references<sup>1,5,10</sup>. The factors  $\frac{\partial B_{mm}}{\partial a}$  and  $\frac{\partial \lambda}{\partial a}$  relate the propagation of the crack front to the local pointwise change of the mode-mixity ( $B_{mm}$ ) and the equivalent one-dimensional displacement jump ( $\lambda$ ), respectively. Therefore, these derivatives can be interpreted as the link between the local damage evolution and the crack propagation. In a self-similar crack growth situation, they can be recognized as the slopes of  $B_{mm}$  and  $\lambda$  in the crack growth direction ( $x_1$ ). Thus, in order to compute  $\frac{\partial B_{mm}}{\partial x_1}$  and  $\frac{\partial \lambda}{\partial x_1}$  the propagation direction must be identified. This is done by means of the Growth Driving Direction (GDD) concept presented in Reference<sup>10</sup> and Section 2.4.1. The crack growth rate ( $da/dN$ ) is evaluated from delamination propagation tests (see Section 3.1.1). The strength of this method is that, any phenomenological expression for the  $da/dN$  that is a function of the energy release rate ( $\mathcal{G}$ ) can be easily included in the simulation. In this case, the crack growth rate is evaluated by:

$$\frac{da}{dN} = \begin{cases} A \left( \frac{\mathcal{G}_{max} (1-R)}{\mathcal{G}_c} \right)^p & \text{for } \mathcal{G}_{th} < \mathcal{G}_{max} < \mathcal{G}_c \\ 0 & \text{for } \mathcal{G}_{max} \leq \mathcal{G}_{th} \end{cases} \quad \text{Eq. 2-14}$$

where  $\mathcal{G}_{max}$  is the maximum cyclic energy release rate measured using the  $J$ -integral approach (more information can be found in Reference<sup>11</sup>),  $R$  is the load ratio, defined as:

$$R = \sqrt{\frac{\mathcal{G}_{min}}{\mathcal{G}_{max}}} \quad \text{Eq. 2-15}$$

and  $\mathcal{G}_{th}$  is the energy release rate threshold below which no propagation occurs. The use of fracture mechanics parameters for the characterization of the fatigue loading is highly motivated by Paris and co-workers' achievements in the characterization of fatigue crack growth in metals<sup>18</sup>. Moreover, since the calculation of the SIF in inhomogeneous materials, such as laminated composites, may be challenging,  $\mathcal{G}$  has become the preferred parameter for the modeling of delamination growth.

The dependency of the Paris' law-based parameters ( $A$  and  $p$ ) with the mode mixity is evaluated in terms of the energy release rate ( $\Phi$  - see Eq. 2-12). The formulation from Reference<sup>19</sup> is used:

$$p = \Phi^2(p_{sh} - p_I - p_m) + \Phi p_m + p_I \quad \text{Eq. 2-16}$$

$$\log(A) = \Phi^2 \log\left(\frac{A_{sh}}{A_m A_I}\right) + \Phi \log(A_m) + \log(A_I) \quad \text{Eq. 2-17}$$

where  $p_I$  and  $A_I$  are the parameters for pure mode I,  $p_{sh}$  and  $A_{sh}$  are the parameters for shear mode, and  $p_m$  and  $A_m$  are mode interpolation parameters.

### 2.3.2. Fatigue damage model

One of the main challenges associated with the derivation of the damage rate ( $d\mathcal{D}^e/dN$ ) is that it is a field variable that depends on the crack growth rate ( $da/dN$ ), which is a scalar variable. In order to handle this challenge, a condition is applied, which states that the distributions of tractions and displacement jumps within the damage process zone are unchanged in the shift between quasi-static loading and fatigue loading or vice versa (see Figure 2-5). This condition is applied because it implies that the  $(\mu, \lambda)$  relation defined by the quasi-static model is maintained during fatigue-driven crack growth (see Reference<sup>5</sup> for further details). In Figure 2-5.a), the unloaded and undamaged cohesive interface is shown. In Figure 2-5.b), the load is increased during the quasi-static ramping phase and the point marked with a cross is confined within the Fracture Process Zone (FPZ). In Figure 2-5.c), the crack has now propagated in the fatigue phase. In Figure 2-5.d), the value of the total specific work ( $\omega_{tot}$ ) at the point marked with a cross is then equal to the energy release rate ( $\mathcal{G}$ ) evaluated with the  $J$ -integral. In order to apply the condition that the distributions of tractions and the displacement jumps within the damage process zone are unchanged in the shift between quasi-static loading and fatigue loading, the tractions drop to zero at the opening traction–displacement relation where  $\omega_{tot} = \mathcal{G}$ . In order to ensure that the traction is reduced to zero when the total specific work  $\omega_{tot}$  (a field variable) is equal to the energy release rate  $\mathcal{G}$  (a scalar variable), the following criterion for full damage is applied:

$$\text{if } \omega_{tot} > \mathcal{G} \quad \text{then} \quad \mathcal{D}^e = 1 \quad \text{Eq. 2-18}$$

In Figure 2-5.e), the fatigue phase is still running but the point marked with a cross is not able to withstand any traction because it is fully damaged.

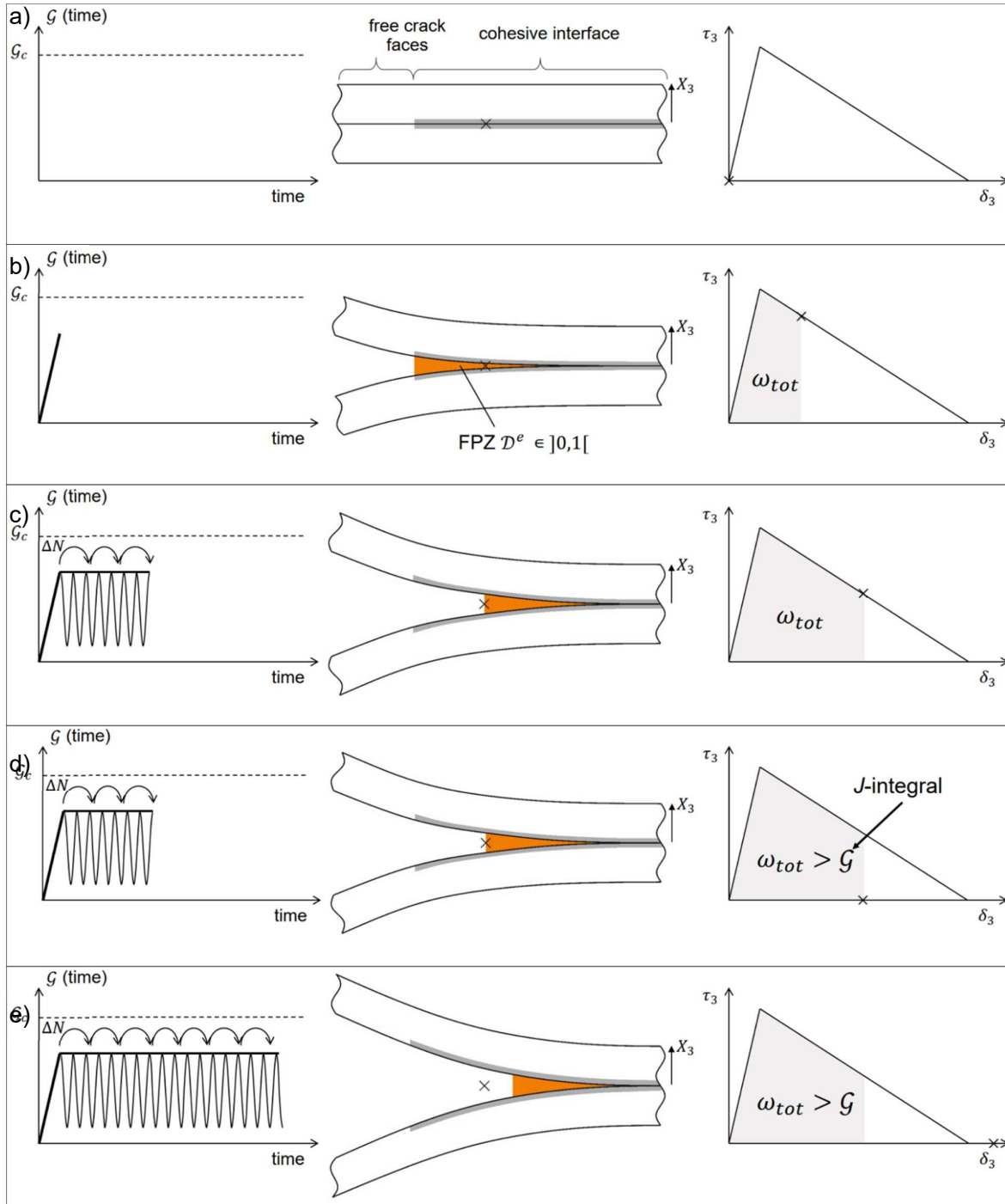


**Figure 2-5. A crack loaded in pure mode I, which exemplifies the condition that the distributions of tractions and the displacement jumps within the damage process zone are unchanged in the shift between quasi-static loading and fatigue loading or vice versa.**

## 2.4. Arbitrarily shaped delamination fronts

As previously noted, the model requires an efficient identification of the crack propagation direction and an accurate means of calculating the mode-decomposed energy release rates for its application to 3D simulation of arbitrarily-shaped delamination fronts. In the following, the concept of GDD to identify the crack propagation direction is briefly described. In addition, a numerical procedure to evaluate the mode-decomposed  $J$ -integral in curved delamination fronts is presented.

### 2.4.1. Growth driving direction

As seen in Section 2.3.1, the rate of change of the mode-mixity ( $B_{mm}$ ) and the equivalent one-dimensional displacement jump ( $\lambda$ ) with crack extension (in Eq. 2-13) is approximately computed as the slopes of these quantities in the propagation direction  $\frac{\partial B_{mm}}{\partial x_1}$  and  $\frac{\partial \lambda}{\partial x_1}$ . Thus, in order to compute these slopes, which are essential in simulations of 3D structures with arbitrarily shaped fronts, it is necessary to identify the crack propagation direction.

In the framework of LEFM, the propagation direction is assumed to be the normal direction to the crack front, where the crack front is the line separating the uncracked and cracked parts (see Figure 2-6.a). In contrast to LEFM, the CZM technique accounts for a band of damaged interface of variable length, called the fracture process zone, FPZ (light grey band in Figure 2-6.b). Therefore, the propagation direction, understood as the normal to the crack front line, cannot be defined in the CZM.

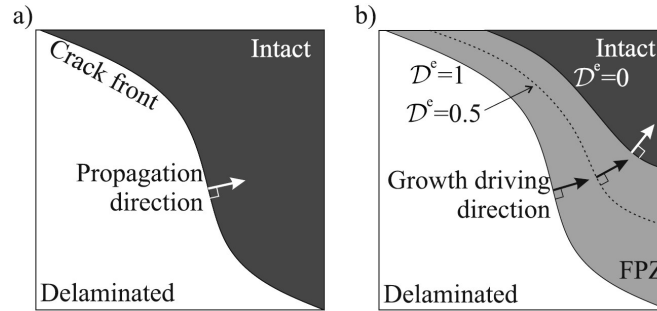


**Figure 2-6. a) The propagation direction is assumed to be the normal direction to the crack front in the LEFM framework. b) The growth driving direction is assumed to be the normal direction to a damage isoline in the CZM framework<sup>10</sup>.**

The concept of Growth Driving Direction (GDD) postulates that the crack propagates in the direction where energy in the cohesive interface is dissipated at the highest rate relative to the fracture toughness. This is equivalent to say that the GDD is the direction of the minimum gradient of energy-based damage:

$$-\nabla \mathcal{D}^e \quad \text{Eq. 2-19}$$

Polar coordinates are most appropriate when looking for a direction from a pole (see Figure 2-7). Thus, the GDD can be found by identifying the angle  $\varphi$  that minimizes the slope of  $\mathcal{D}^e$  with respect to the radial coordinate  $\rho$ :

$$\min_{\varphi} \frac{\partial \mathcal{D}^e}{\partial \rho} \quad \text{Eq. 2-20}$$

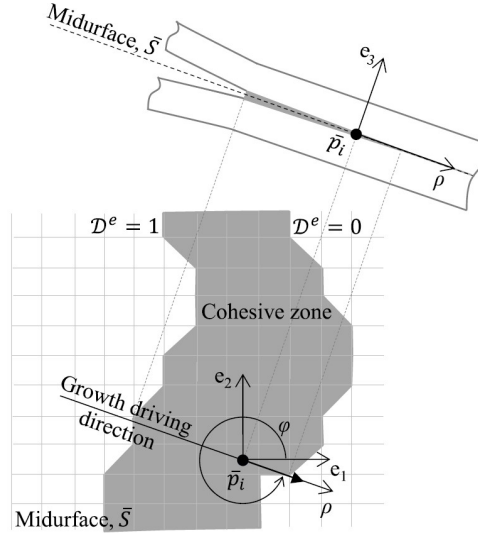


**Figure 2-7. GDD evaluated at point  $\bar{p}_i$  is embedded in the tangential plane spanned by the local Cartesian coordinates  $e_1$  and  $e_2$ <sup>11</sup>.**

Since the constitutive law is formed by an initial elastic region, before damage initiation, another criterion to identify the GDD in the elastic regime must be used. The following criterion is also active before the initiation of the degradation process, and is the selected criterion to be implemented in the fatigue method developed in this Task T5.1:

$$\min_{\varphi} \frac{\partial (\omega_{tot}/g_c)}{\partial \rho} \quad \text{Eq. 2-21}$$

Both the conservative and the non-conservative work are computed in Eq. 2-21. This implies that, as soon as two initially coinciding points separate from each other ( $\lambda > 0$ ), some elastic energy is stored that makes this criterion active before damage onset. Once the damage is initiated, both criteria lead to the same GDD solution. Note that the total specific work ( $\omega_{tot}$ ) is computed relative to the loading mode dependent fracture toughness ( $g_c$ ). This makes the criterion dependent the mode mixity.

### 2.4.2. J-integral

The  $J$ -integral is a suitable method for calculating the mode-decomposed energy release rates in arbitrarily shaped delamination fronts because its domain-independence is employed to reduce the integration domain to the cohesive interface, and reduce it to a line integral (see Figure 2-8). The GDD criterion, which takes into account the loading state at each point, is used to render the integration paths and to decompose the  $J$ -integral into loading modes.



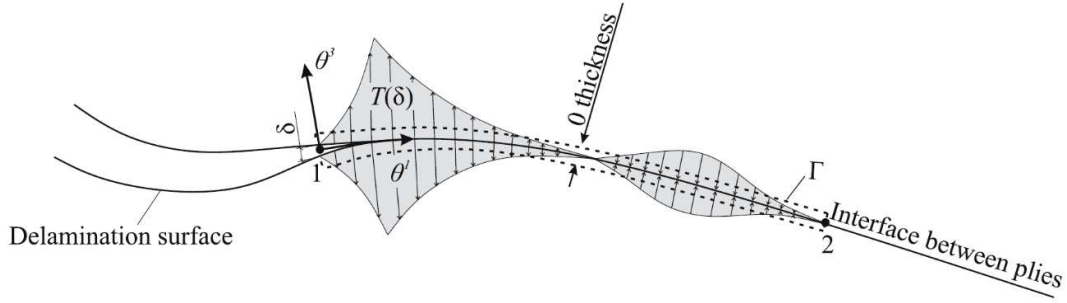


**Figure 2-8.** The integration path  $\Gamma$  (dashed line) is reduced to the zero-thickness cohesive interface<sup>11</sup>.

$\theta_i$ ,  $i = 1, 2, 3$  is an orthogonal curvilinear coordinate system with origin at a given point along the crack front. This local coordinate system is oriented such that  $\theta^3$  is normal to the crack surface,  $\theta^2$  is the coordinate along the crack front and  $\theta^1$  is the direction of crack propagation, which is always tangent to the crack surface and perpendicular to  $\theta^2$  and  $\theta^3$ .

Note that the integration domain of the  $J$ -integral is a slice of infinitesimal thickness lumped into the delamination interface. Thus, the integration domain is reduced to a path contained in the delamination interface that follows the direction of crack propagation ( $\theta^1$  – see Figure 2-8). Moreover, the  $J$ -value of each integration path is unique and is obtained when the integration path is covered in its entirety, i.e., going through the entire cohesive zone, from the completely damaged zone (point 1 in Figure 2-8, with zero cohesive stress) to the end of the zone in elastic regime (point 2 in Figure 2-8, also with zero cohesive stress).

In its FE implementation, the  $J$ -integral is computed at all the integration points and approximated by numerical integration as:

$$J_I = - \sum_t \frac{1}{2} h^t \left[ \left( \tau_3 \frac{\partial \delta_3}{\partial x_1} \right) \Big|_t + \left( \tau_3 \frac{\partial \delta_3}{\partial x_1} \right) \Big|_{t+1} \right] \quad \text{Eq. 2-22}$$

$$J_{II} = - \sum_t \frac{1}{2} h^t \left[ \left( \tau_1 \frac{\partial \delta_1}{\partial x_1} \right) \Big|_t + \left( \tau_1 \frac{\partial \delta_1}{\partial x_1} \right) \Big|_{t+1} \right] \quad \text{Eq. 2-23}$$

$$J_{III} = - \sum_t \frac{1}{2} h^t \left[ \left( \tau_2 \frac{\partial \delta_2}{\partial x_1} \right) \Big|_t + \left( \tau_2 \frac{\partial \delta_2}{\partial x_1} \right) \Big|_{t+1} \right] \quad \text{Eq. 2-24}$$

where  $\tau_k$  are the cohesive traction components expressed in the local coordinate system oriented according to the GDD and  $\frac{\partial \delta_k}{\partial x_1}$  are the oriented slopes of the displacement jump components in the GDD.  $h^t$  is the Euclidean distance between consecutive points along the integration path.

### 3. Methodology

After the development of the 3D progressive delamination method, the actions carried out in Task 5.1 can be classified into two main disciplines: mechanical testing (reported in Section 3.1) and numerical modelling (reported in Section 3.2).

In turn, the testing was devoted to two proposes: the characterization of the material properties to input the numerical method (see Section 3.1.1) and the testing of a demonstrator specimen to obtain experimental results against which to validate the method (see Section 3.1.2). The work related to numerical modelling was also divided into two sub-tasks: implementing the developed fatigue damage method the finite element code SAMCEF (see Section 3.2.1) and simulating the delamination demonstrator (see Section 3.2.3).

#### 3.1. Mechanical testing

##### 3.1.1. Characterization of material properties

The test specimens were made of a glass fibre reinforced (GFR) epoxy composite material with a unidirectional (UD1340) architecture based on non-crimp fabrics with backing fibres in the  $\pm 45^\circ$  directions (Biax100). The weight percentage of backing in the fibre was 7% and the area weight was 1.483 kg/m<sup>2</sup>.

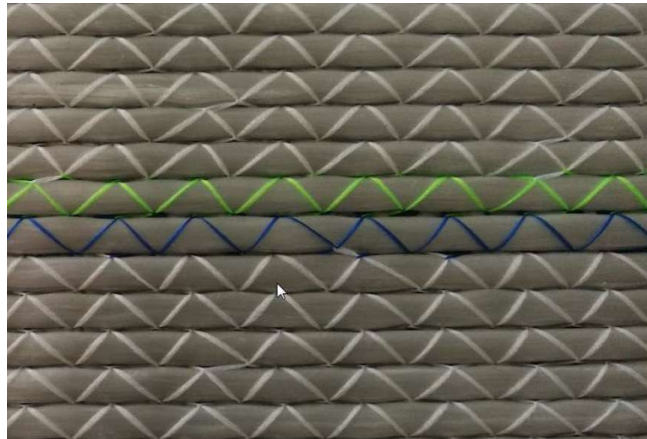


Figure 3-1. Picture of a dry ply with a detailed view of the stitching.

A characterization campaign addressed to obtain the required material properties to input the numerical method presented in Section 2 was carried out. The elastic properties of the ply were characterized by SGRE, while the fracture properties of the interface between plies were characterized by AAU. The properties obtained are listed in Table 3-1.

Table 3-1. Material properties to input the numerical method.

PROPERTY		SYMBOL
ELASTIC PROPERTIES OF THE PLY	Longitudinal Young's modulus	$E_{11}$
	Transversal Young modulus	$E_{22}$
		$E_{33}$
	Shear modulus in the longitudinal planes	$G_{12}$
		$G_{13}$
	Shear modulus in the transversal plane	$G_{23}$
		$\nu_{12}$

*Quasi-static*

FRACTURE PROPERTIES OF THE INTERFACE	Poisson's coefficients in the longitudinal planes	$\nu_{13}$	
	Poisson's coefficients in the transversal plane	$\nu_{23}$	
	Mode I fracture toughness	$G_{Ic}$	
	Mode I Paris' law coefficient	$A_I$	
	Mode I Paris' law exponent	$p_I$	<i>Fatigue</i>
	Mode I energy release rate threshold	$G_{Ith}$	

### ***Characterization of the elastic properties of the ply***

The value and procedure followed to obtain the elastic properties of the ply material are outlined in Table 3-2.

**Table 3-2. Values and procedures followed to obtain the elastic properties of the ply material**

$E_{11} = 4.796 \cdot 10^{10} \text{Pa}$
ISO 527-1, ISO 527-5 Type A
Mean value
Standard deviation = 0.29 GPa
$E_{22} = 1.397 \cdot 10^{10} \text{Pa}$
Estimated value <sup>4</sup>
$E_{33} = 1.318 \cdot 10^{10} \text{Pa}$
Estimated value <sup>4</sup>
$G_{12} = 4.27 \cdot 10^9 \text{Pa}$
Measured from a similar material, using ASTM D7078
Mean value
Standard deviation = 0.151 GPa
$G_{13} = 2.2 \cdot 10^9 \text{Pa}$
Estimated value <sup>4</sup>
$G_{23} = 1.5 \cdot 10^9 \text{Pa}$
Estimated value <sup>4</sup>
$\nu_{12} = 0.316$
Measured from a similar material, using ISO 527-1, ISO 527-5 Type A
Mean value
Standard deviation = 0.016
$\nu_{13} = 0.251$
Estimated value <sup>4</sup>
$\nu_{23} = 0.335$
Estimated value <sup>4</sup>

### ***Characterization of the fracture properties of the interface between plies***

For the characterization of the fracture properties, DCB specimens were used. Specimens were manufactured (stacked, cured and cut) by SGRE according to the design made by AAU. The specimen's dimensions and lay up are specified in Figure 3-2.

<sup>4</sup> Values are based on correlation with previous full-scale blade and component test as well as in-house proprietary software tools at SGRE.

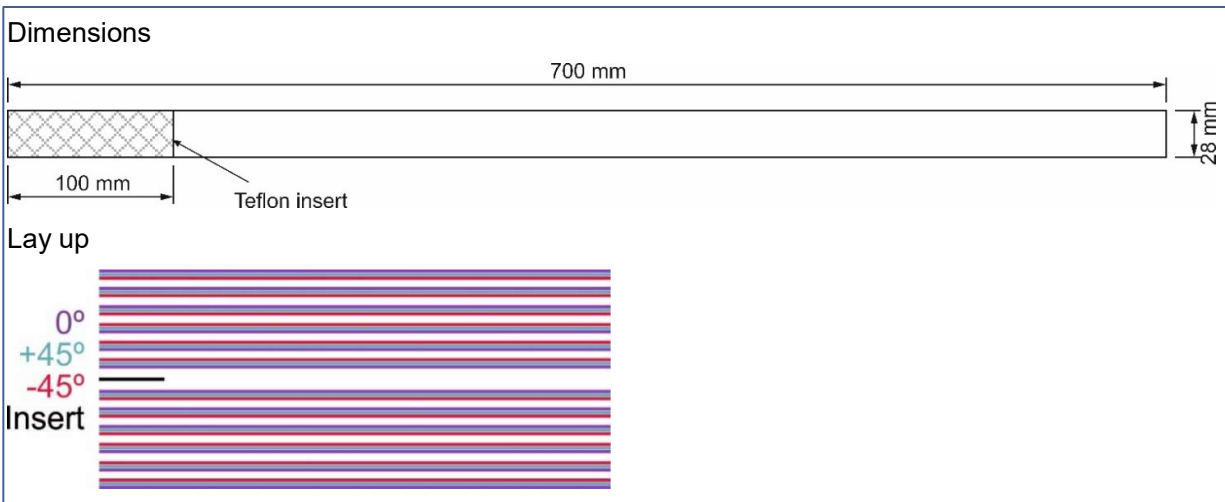


**Figure 3-2. Dimensions and lay up of the DCB specimens used for the characterization of the fracture properties.**

Quasi-static testing to obtain the mode I fracture toughness,  $G_{Ic}$

For quasi-static-driven delamination testing of DCB specimens, the test fixture developed by AAU presented in Reference<sup>9</sup> was used. The test fixture, shown in Figure 3-3, produces bending moments on the arms of the DCB specimens based on a pure tensile loading input from the electro-mechanical testing machine (Zwick 100 kN), thus using the actuation and high quality data acquisition system already available. The concept of the test fixture is based on the principle from Reference<sup>20</sup>, where a string pulley system can introduce pure bending moments on a DCB specimen. The developed test fixture is designed such that unwanted effects from large displacements and rotations are minimized, which imply that the test fixture can be used to test more compliant and thereby thinner DCB specimens.

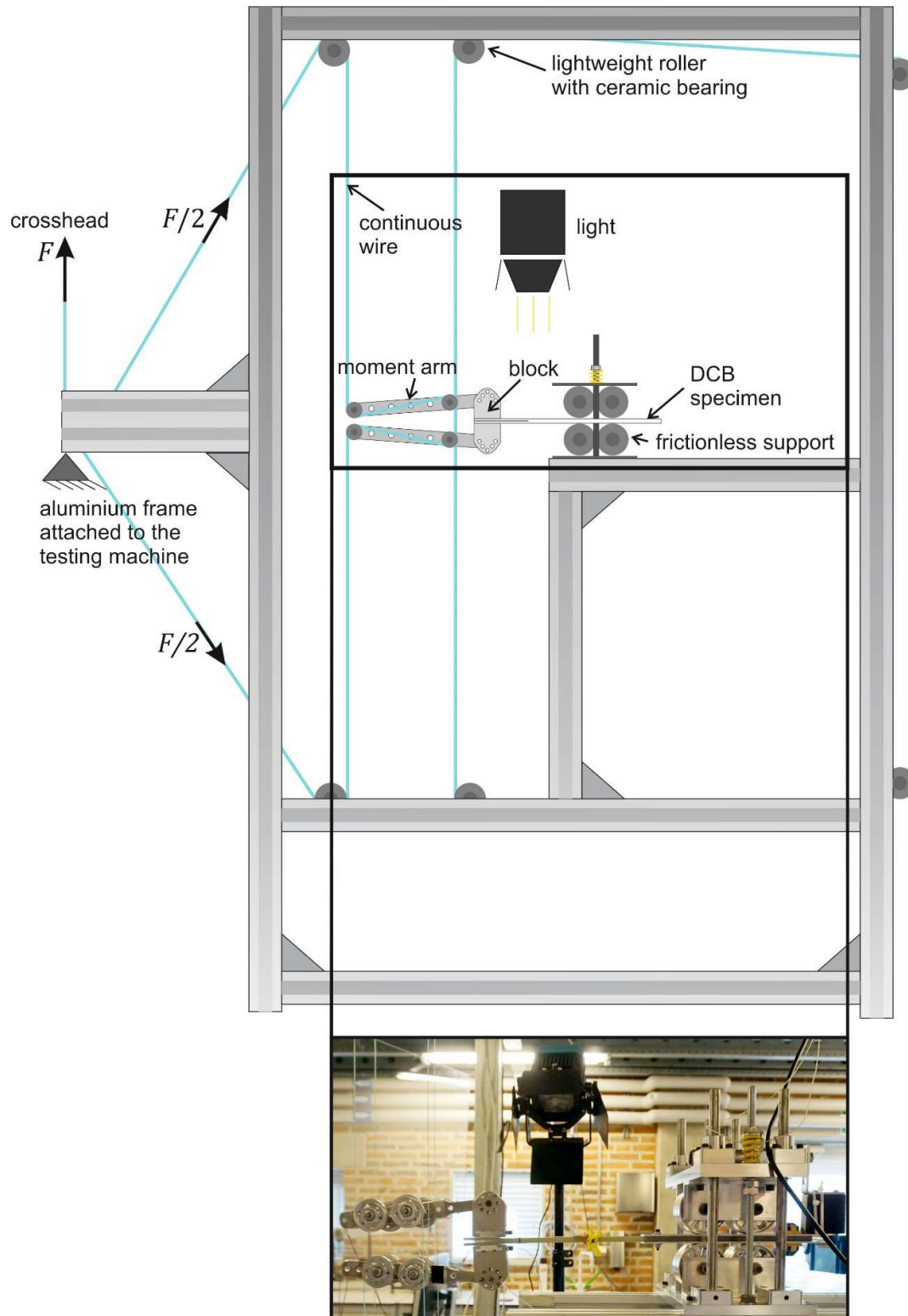


**Figure 3-3. Overview of test fixture for bending test of DCB specimen with bending moments.**

The basic outline of the fixture is as follows. The DCB specimen is mounted in a frictionless support achieved by lightweight rollers and ceramic bearings. In between the DCB specimen and roller support two aluminium plates are placed to ensure a smooth rolling surface. Two moment loading arms with rollers are attached to the specimen. The applied force couple to each of the moment loading arms is achieved by a wire and roller system using a single continuous wire, which ensures

a constant wire force and thus identical force on each roller on the moment loading arm. The force,  $F$ , measured at the load cell, results in vertical, equal and opposite forces of magnitude  $F/2$  that act transversely on the DCB arms and result in a pure bending moment given by

$$M = \frac{F}{2}s \quad \text{Eq. 3-1}$$

where  $s$  is the horizontal distance between the two points of load application (wires around rollers at the moment arms). In order to calculate  $s$ , the angle of each loading arm is measured using inclinometers. A pretensioned braided Dyneema rope is used as wire due to its low weight, low friction, low bending stiffness, high tensile stiffness, and high strength.

The mode I energy release rate,  $G_{Ic}$ , for the moment loaded DCB specimen shown in Figure 3-3 can be determined based on the  $J$ -integral approach<sup>21</sup> and assuming plane strain conditions:

$$G_{Ic} = \frac{12(1 - \nu^2)M^2}{Eh^3b^2} \quad \text{Eq. 3-2}$$

where  $h$  is the height of each beam,  $b$  is the width of the DCB specimen,  $E$  is Young's modulus,  $\nu$  is the Poisson's ratio, and  $M$  is the applied moment on each arm of the DCB specimen.

Fatigue testing to obtain the Paris' law based parameters for the mode I crack growth rate curve,  $A_I$ ,  $p_I$ ,  $G_{Ith}$

Fatigue testing was aimed at obtaining the crack growth rate curve (see Figure 3-4), which relates the rate of crack propagation in mm/cycle with a Paris' law-based function of the maximum cyclic energy release rate (see Eq. 2-14).

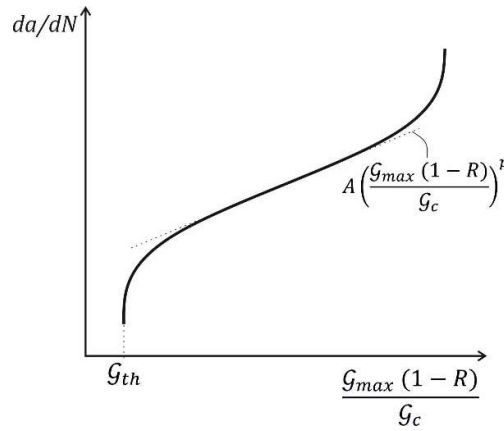


**Figure 3-4. Schematic crack growth rate curve**

For fatigue-driven delamination testing of DCB specimens, a more compact pure mode I moment test fixture than the previously presented was used. The test fixture developed in Reference<sup>22</sup> was used as inspiration and the design was adapted to the available electro-mechanical testing machine for static and fatigue testing (Instron Electropuls 10kN) and manufactured by AAU. A system of pulleys and wires was used to apply a bending moment to each DCB arm, as shown schematically in Figure 3-5. A prescribed displacement at the crosshead results into a reaction force,  $F$ , applied to each pulley at point A and the resulting tension in each vertical segment of wire looped around the pulleys is then  $F/2$ . Therefore, at points B and C, equal and opposite forces of magnitude  $F/2$  act transversely on the DCB arm that result in a pure mode I bending moment given by Eq. 3-1. Notice that, in contrast to the previous testing rig, this set up uses four separate wires.

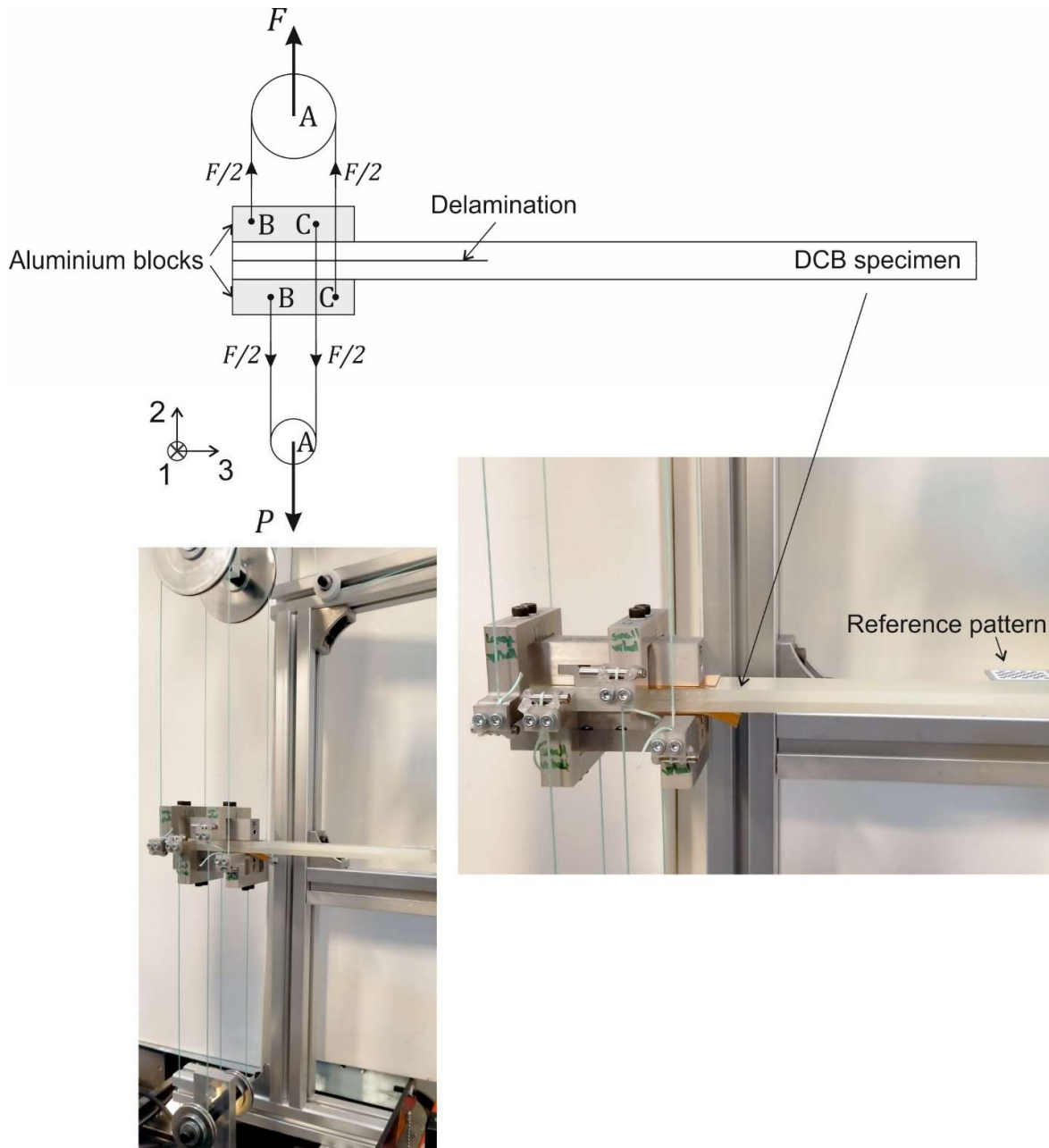


**Figure 3-5. Overview of the compact test fixture for bending test of DCB specimen with bending moments.**

Tests were run sinusoidally at constant-amplitude displacement with a load ratio,  $R$ , of 0.1 and a frequency of 5 Hz. For a constant-amplitude displacement at the crosshead, the arm rotation is constant with crack propagation and can be obtained geometrically assuming that the wire elongation can be neglected. Thus, the use of inclinometers to determine  $s$ , the horizontal distance between the two points of load application, was avoided. The reaction force,  $F$ , was measured at the load cell.

An automated digital image-based tracking method<sup>23</sup> was used to track the crack front position along the fatigue test (see Figure 3-6). This method exploits the increased intensity of diffuse reflected light of the irregular surface of the newly formed crack area to highlight the location of the newly formed crack. The crack tip at a certain number of loading cycles was taken as the averaged crack length across the specimen width. A PointGrey Blackfly (monocolour  $2,448 \times 2,048$  pixels ethernet camera) with an Edmund optics 75 mm double Gauss lens was filming the top of the specimen, and two NILA ZAILA lights were applied on the same side of the specimen as the camera location. The

lights were angled such that the light was reaching the specimen at an angle of approximately  $45^\circ$ . Changes in both the relative position and orientation of the camera and/or specimen were compensated by using a reference pattern attached to the specimen. The reference pattern was flat and placed such that it is coplanar with the top surface of the undamaged part of the specimen. The camera was synchronised with the tensile testing machine, and the images were acquired at intervals of 10 fatigue cycles.

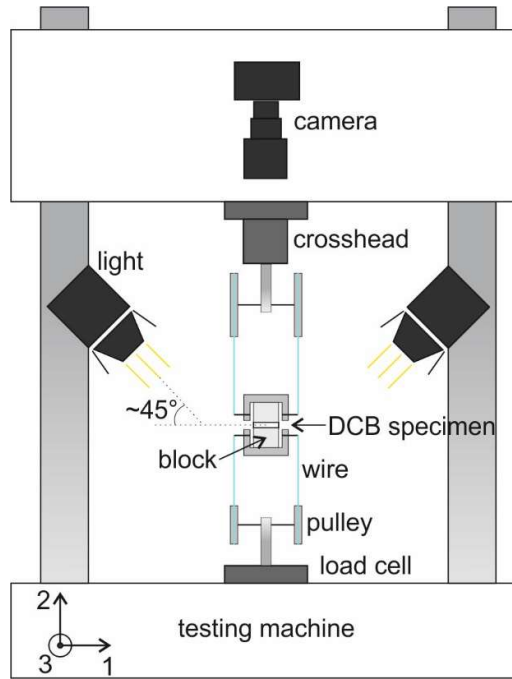


**Figure 3-6. Layout of the test setup with digital image acquisition to track the delamination front.**

When images are used to determine the location of the crack front, the cracked area appears brighter (a higher greyscale value) than the uncracked area, and it is the only significant change between images acquired at different stages of the test. In order to enhance the crack in the images showing crack propagation, a reference image of the uncracked specimen (Figure 3-7.a) is divided pixel by pixel by the image of interest (Figure 3-7.b). After scaling of the greyscale values and removing the noise by using a disc-formed structuring element of 4 pixels radius to morphologically close the image, the image is simplified such that each pixel only represents one of two categories: i) crack or ii) no crack. This is done by defining a threshold greyscale value below which the pixels are categorised as belonging to the crack (Figure 3-7.c). In order to systemise the definition of the threshold greyscale value and to make it insensitive to the histogram of the morphologically closed image, the K-means clustering algorithm<sup>24</sup> is used.



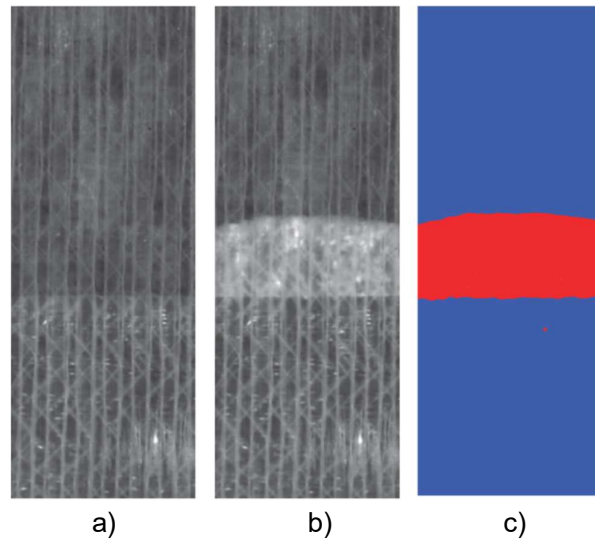


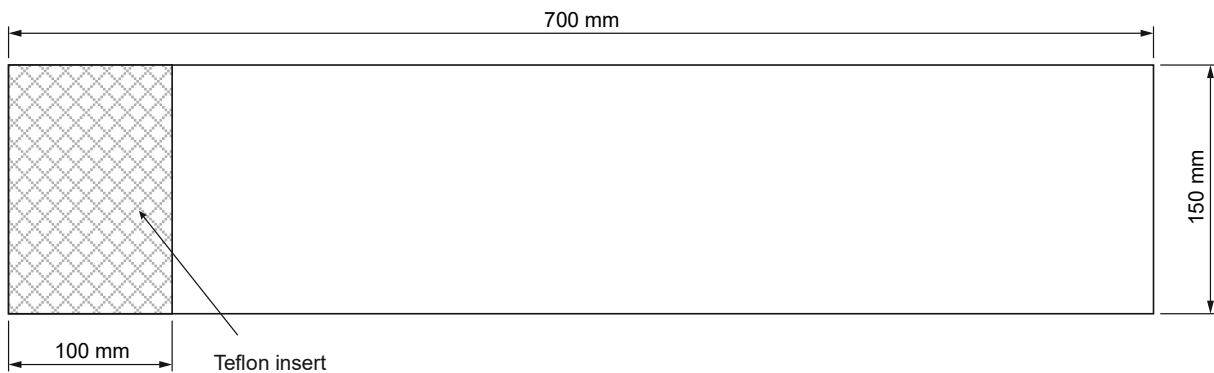
**Figure 3-7. (a) Reference image (no crack propagation). (b) Image after crack. (c) Categorisation by greyscale threshold<sup>23</sup>.**

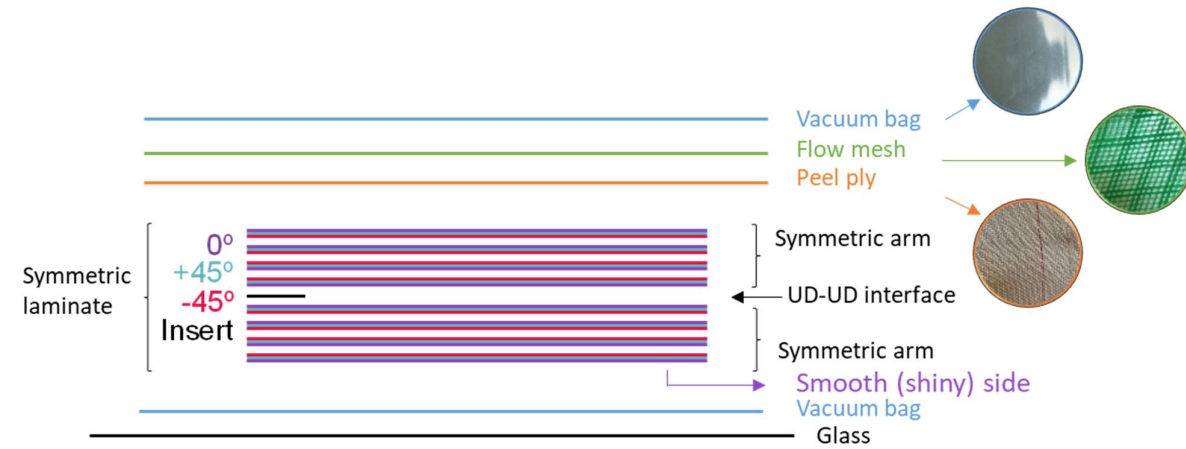
The crack growth rate  $da / dN$  is determined by fitting a linear function to all data points within a moving fitting window of 1,000 cycles  $\times$  2 mm, which is centred around the point of interest<sup>23</sup>, and the energy release rate is derived using Eq. 3-2.

### 3.1.2. Testing of delamination demonstrator

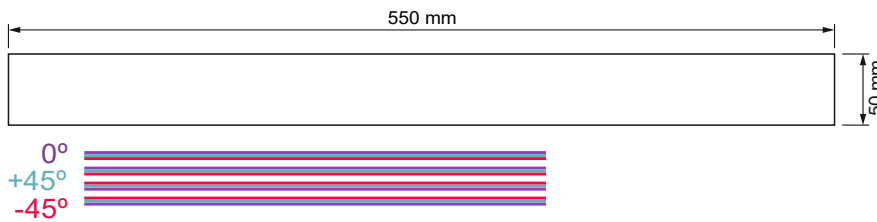
The test specimen is a DCB manufactured by Vacuum Assisted Resin Transfer Molding (VARTM) and consists of eight plies at  $0^\circ$  with an initial straight delamination front made by a Teflon insert at the mid-plane. Two reinforcements, made of four plies of the same material and orientation, are bonded on top and bottom sides of the specimen in order to promote curved delamination front (see Figure 3-8). The partially reinforced specimen generates a rich phenomenology of crack advance in terms of varying crack growth rate and crack front shape.

#### Plate





### Reinforcement



### Arrangement

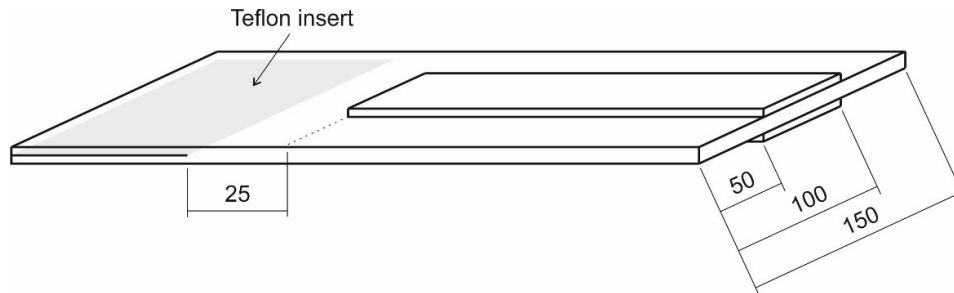


**Figure 3-8. Dimensions and arrangement of the reinforcement of the partially reinforced DCB specimen (units in mm).**

The different elements (plate and reinforcements) of the demonstrator specimen were manufactured (stacked, cured and cut) by SGRE according to the design made by AAU. The reinforcements were bonded to the plate at the facilities of AAU using the 2-component epoxy adhesive Permalock EP 708. In order to ensure an even distribution of the adhesive through the entire plate-reinforcement interface, a vacuum bag was used. First, the adhesive was manually applied on both adherents with a two component cartridge gun, making sure that there was enough adhesive to cover the entire surfaces (see Figure 3-9). Then, the reinforcement was put in place and aligned by the aid of guiding pins in the plate and reinforcement. The whole specimen was then introduced into a vacuum bag, with the outlet positioned near the reinforcement edge closest to the initial delamination. This was done in order to make sure that there is enough adhesive at the edge, where the abrupt change in stiffness supplied by the reinforcement causes stress concentration at the bond interface.

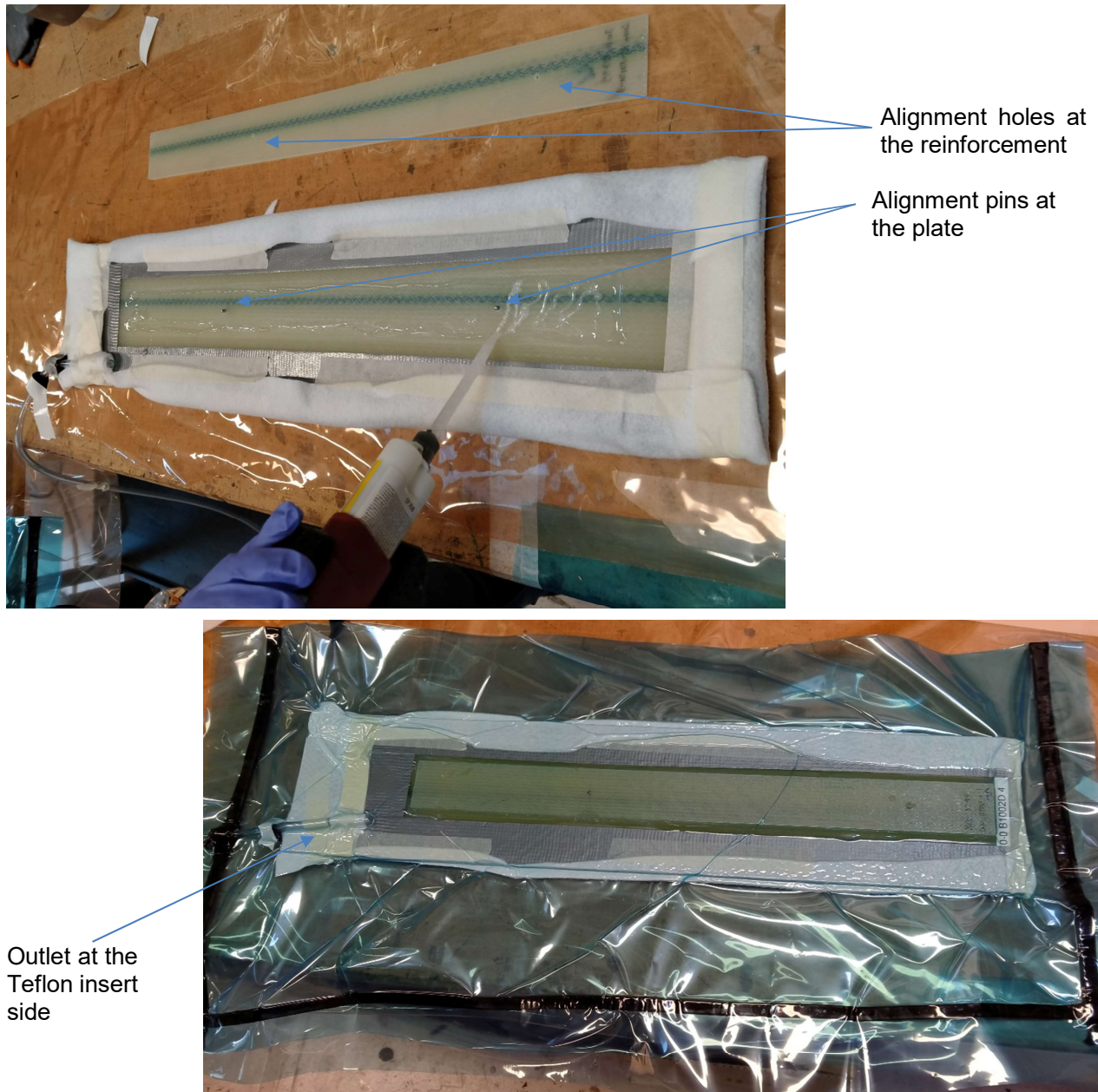


**Figure 3-9. Bonding of the reinforcement to the plate in the demonstrator specimen.**

Fatigue tests on the demonstrator specimen were done using the test fixture for delamination test of DCB specimen with bending moments shown in Figure 3-3. Tests were run sinusoidally at constant-amplitude moment with a load ratio,  $R$ , of 0.1 and a frequency of 2 Hz. A servo-hydraulic testing machine (Schenck 100 kN) was used. The moment control was done by means of the strain measurement on the moment arms. The automated digital image-based tracking method<sup>23</sup> presented in Section 3.1.1 was used to track the crack front position along the fatigue test. The combined experimental set up used for the testing of the demonstrator specimen is sketched in Figure 3-10. Three computers were used for control and data acquisition:

- 1- The testing machine computer was used to control the crosshead displacement to match the target moment as a function of the input from the strain gauge placed on the upper moment arm.

- 2- The data acquisition computer saved data from the strain gauge placed on the lower moment arm and temperature.
- 3- The image acquisition computer received cyclic data from the testing machine, sent the signal to the camera to take a picture every 50 cycles, and received and saved the picture from the camera.

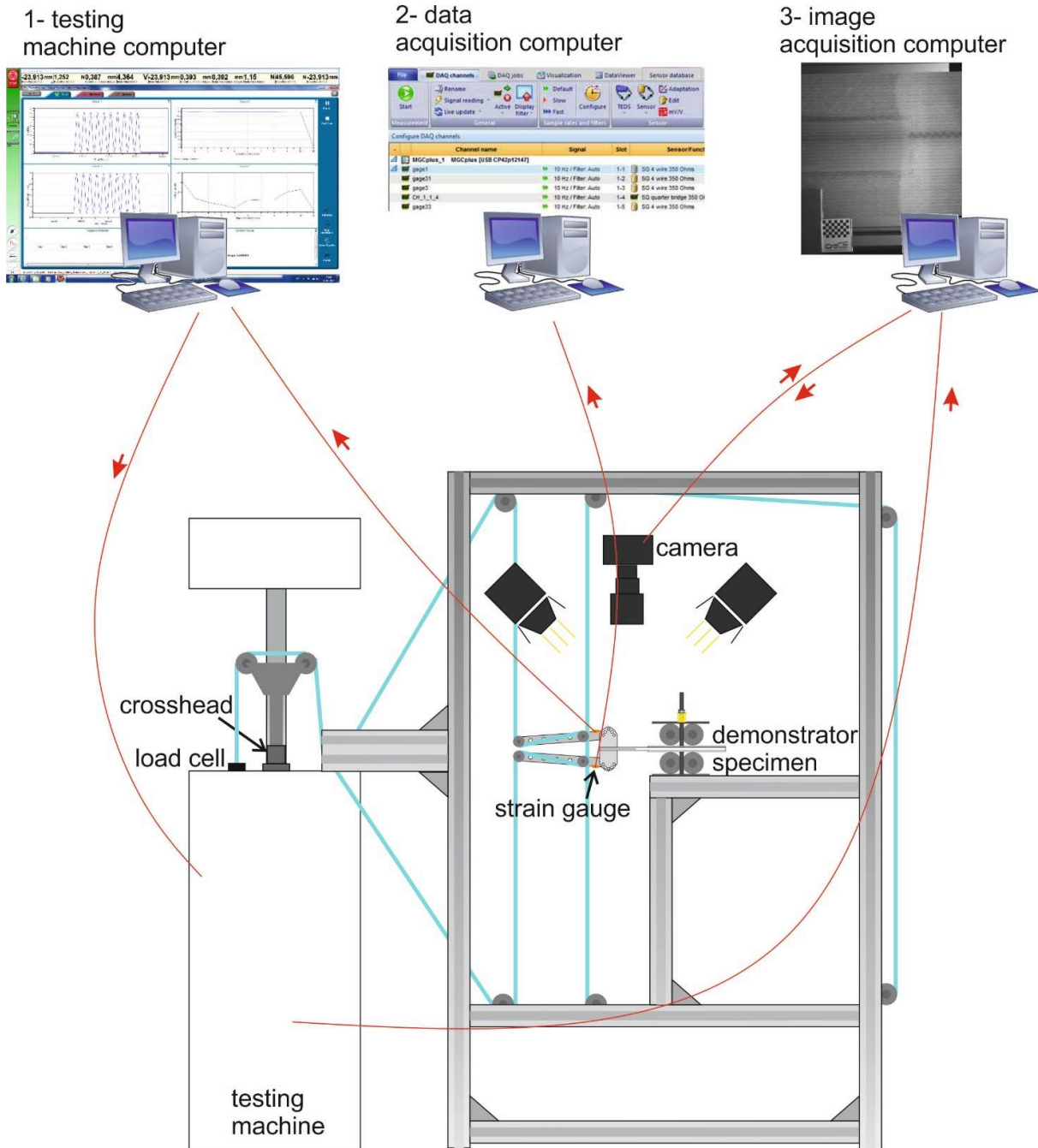


**Figure 3-10. Experimental set up and data flow for the testing of the demonstrator specimen**

Crack front location versus number of cycles was extracted from the automated digital image-based tracking method<sup>23</sup>. A local regression smoothing<sup>25</sup> was used to smooth the detected crack front



throughout the specimen width due to the effect of the adhesive, the reinforcement edge, the stitching colouring, etc. The local regression smoothing process uses a moving average method, with which each smoothed value is determined by neighbouring data points defined within the span. The process is weighted because a regression weight function is defined for the data points contained within the span. A quadratic polynomial model is used in the local regression. A span of 20% of the total number of data points was used.

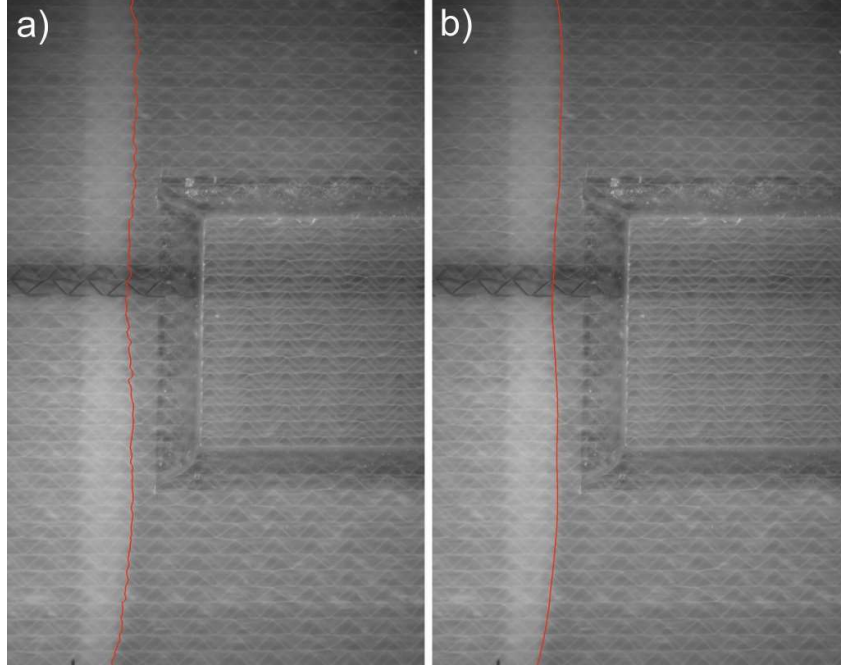


Figure 3-11. Comparison between the crack front tracking a) before and b) after the local regression smoothing.

### 3.2. Numerical modelling

#### 3.2.1. Finite element model implementation in SAMCEF

The model presented in Section 2 was implemented in the Simcenter Samcef solver v1980 as a new behaviour law. In order to improve convergence, two features are usually used for all continuous damage laws implemented in the Samcef solver:

1. An upper limit ( $d_{max}$ ) for the stiffness degrading damage ( $\mathcal{D}^k$ ) that is very close but lower than 1. This is done to avoid elements with null stiffness. Thus, the implemented  $\mathcal{D}^k$  reads:

$$\mathcal{D}^k = \max \left( \min \left( \frac{\lambda_c \langle \lambda - \lambda_o \rangle_+}{\lambda (\lambda_c - \lambda_o)}, d_{max} \right), r \right) \quad \text{Eq. 3-3}$$

where  $r$  is the historical maximum value of  $\mathcal{D}^k$ , or current damage threshold, and  $\langle \cdot \rangle_+$  are the Macaulay brackets.

2. Secondly, a delayed damage strategy that smoothens the transition from the elastic behaviour to damage by applying a low viscosity effect.

$$\dot{\mathcal{D}}^k = \frac{1}{\tau_c} \{1 - \exp(-a_c (\omega - \mathcal{D}^k))\} \quad \text{where } \omega = \frac{\lambda_c \langle \lambda - \lambda_o \rangle_+}{\lambda (\lambda_c - \lambda_o)} \quad \text{Eq. 3-4}$$

where  $\tau_c$  is a time delay characteristic parameter and  $a_c$  is a delay coefficient.

The keywords in the pre-processing module, called Bacon, used to set the material parameters are listed in Table 3-3.

**Table 3-3. Material parameters**

.MAT	I material_number NOM "material_name" BEHA "FATIN"	Behavior selection
	YT ( $k$ )	Penalty stiffness (see Eq. 2-1)
	XT ( $\tau_{Io}, \tau_{sho}$ )	Interface strength in mode I and shear (see Eq. 2-8)
	DCOU ( $\eta$ )	Mixed mode exponent (see Eq. 2-7)
	GC ( $G_{Ic}, G_{shc}$ )	Critical energy release rates in mode I and shear (see Eq. 2-7)
	TAU ( $\tau_c$ )	Characteristic delay effect time (see Eq. 3-4)
	ADEL ( $a_c$ )	Delay effect coefficient (see Eq. 3-4)
	DDEN ( $d_{max}$ )	Upper limit for the stiffness based damage variable ( $\leq 1$ ) (see Eq. 3-2)
	CPAR ( $A_I, A_{sh}, A_m$ )	Paris' law coefficients in mode I and shear, and mixed mode interpolation parameter (see Eq. 2-17)
	MPAR ( $p_I, p_{sh}, p_m$ )	Paris' law exponents in mode I and shear, and mixed mode interpolation parameter (see Eq. 2-16)

In order to avoid simulating all fatigue cycles, since this would mean prohibitive CPU time especially for the simulation of high cycle fatigue, a load envelope approach is followed. Thus, the fatigue damage is updated at certain number of cycles. The damage at a given simulation time is obtained by integration of the damage rate for a given number of cycles (see Section 2.3.1). The cycle interval is calculated using a cycle jump algorithm. The algorithm implemented in Samcef consists on 3 steps:

- **step 1:** compute one fatigue cycle during which the fatigue damage does not evolve.
- **step 2:** at the end of step 1, the number of cycles that will be used for the integration of the damage rate, called cycle jump, is selected. This is done by a loop on all the integration points.
- **step 3:** update the damage at all the integration points when the cycle jump is known.

During step 2, the computation of the local cycle jump, NJUMP1, is obtained by dividing the target crack length extension selected by the user,  $\Delta a$ , by the local crack growth rate,  $\frac{da}{dN}$ , at all the integration points in the model:

$$NJUMP1 = \frac{\Delta a}{\frac{da}{dN}} \quad \text{Eq. 3-5}$$

NJUMP1 is stored for every integration point.

In order to avoid too small cycle jumps, which would be computationally ineffective, and to avoid too large cycle jumps, in order to preserve numerical stability and accuracy, a statistical strategy is used.

A maximum cycle jump, NCYMAX, is selected by the user, as well as the number of intervals in which the range from 0 to NCYMAX is divided. A NJUMP1 distribution is made by counting the number of integration points in the model with a NJUMP1 within each interval. All NJUMP1 that are higher than NCYMAX are not taken into account.

From this distribution, a repartition function (see Figure 3-12) is built. The global cycle jump, NJUMP, is the value such that a given percentage (PERCYC) of integration points is below NJUMP.

In order to compute between which intervals NJUMP will be, NJ1 and NJ2 are the number of jumps at the beginning and end of the interval and NP1 and NP2 the ordinate at the beginning and end of the interval. Then, NJUMP is computed as:

$$\text{NJUMP} = \text{NJ1} + (\text{PERCYC} * \text{NPOINT} - \text{NP1}) * (\text{NJ2} - \text{NJ1}) / (\text{NP2} - \text{NP1}) \quad \text{Eq. 3-6}$$

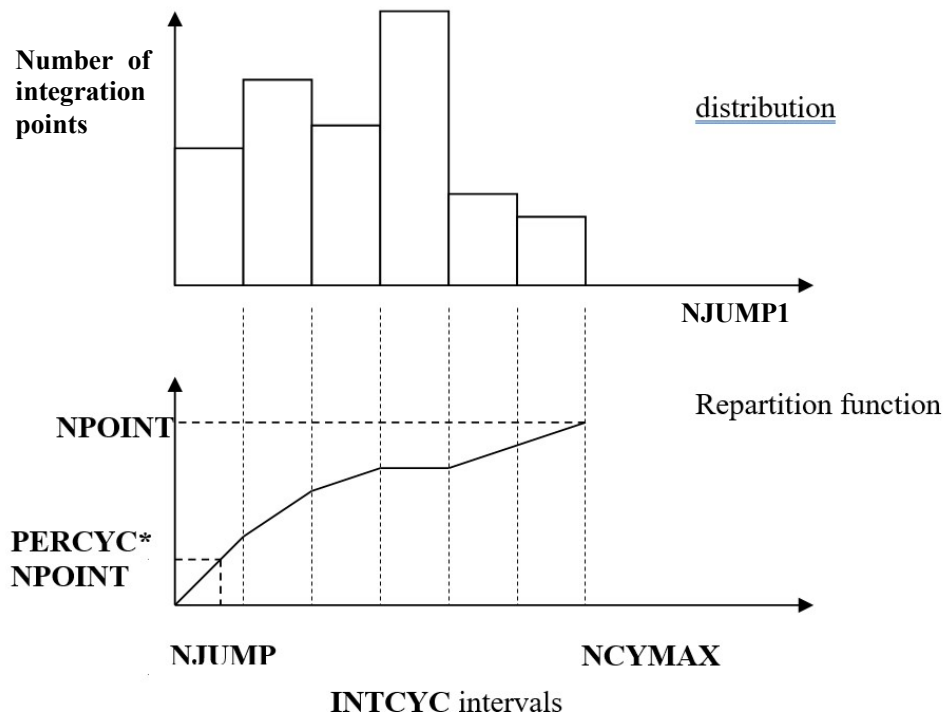


**Figure 3-12: Distribution and repartition function used to identify the global cycle jump, NJUMP**

The parameters in Bacon, and their default values between brackets, involved in the cycle jump algorithm are provided in Table 3-4:

**Table 3-4.: Parameters involved in the cycle jump algorithm**

.SUB	I subcase number	
	TYJUMP [0]	=0 deactivation =1 activation cycle jump algorithm
	NCYCL [10 <sup>8</sup> ]	number of cycles to perform
	CYCMAX [10 <sup>5</sup> ]	value for NCYMAX
	PERCYC [5]	an integer value should be given 5 (5 means 5%)
	JUMA	Maximum value of cycle jump, NJUMAX
	CYCA ( $\Delta a$ )	Limit of crack growth to compute NJUMP1 (see Eq. 3-5)

The available results in the post-processing module and their attributed code value are listed in Table 3-5.

**Table 3-5. Post-processing results**

Code value	Components	Name	Symbol
X356	-	Stiffness-degrading damage	$\mathcal{D}^k$ (see Eq. 2-5)
X499	1	Scalar displacement jump	$\lambda$ (see Eq. 2-2)
	2	Mixed mode ratio	$B_{mm}$ (see Eq. 2-10)
	3	Specific work ratio	$\omega_{tot}/g_c$ (see Figure 2-4)
	4	Energy-based damage	$\mathcal{D}^e$ (see Eq. 2-6)
X847	-	Angle between GDD direction and local direction e1	$\varphi$ (see Eq. 2-21)
X867	1	Mode I component of the J-integral	$J_I$ (see Eq. 2-22)
	2	Mode II component of the J-integral	$J_{II}$ (see Eq. 2-23)
	3	Mode III component of the J-integral	$J_{III}$ (see Eq. 2-24)

Where X can have the values:

- 1: for node-based field output
- 3: for element-based field output
- 9: for element-based field output that is a function of time



### 3.2.2. Validation test case

#### 3.2.2.1. Reinforced ELS test

This test case is used to validate the implementation of the Samcef model of the cohesive law for static loading and the GDD computation. The reference model was implemented and computed with Abaqus and the results were published in Reference<sup>26</sup>. The validation analysis was performed with Samcef solver and compared to the reference results. The test configuration is an End-Loaded Split (ELS) test on a symmetric run-out specimen with a midplane initial defect. A Teflon insert acts as an initial straight delamination (see Figure 3-13). Moreover, the middle width of the specimen is stiffened by bonding CFRP reinforcements on the upper and lower faces. During propagation the crack front shape changes when it approaches the reinforced region. The cohesive elements that model the middle interface are 0.2 mm x 0.5 mm. The boundary conditions are presented in Figure 3-13. The laminate and interface properties used in the simulation are listed in Table 3-6.

**Table 3-6. Laminate and interface properties for ELS test in Section 3.2.2.1**

Laminate properties			Interface properties		
$E_{11}$	154	GPa	$\bar{G}_{Ic}$	0.3	N/mm
$E_{22} = E_{33}$	8.5	GPa	$\bar{G}_{shc}$	3	N/mm
$G_{12} = G_{13}$	4.2	GPa	$\tau_{Io}$	10	MPa
$G_{23}$	3.036	GPa	$\tau_{sho}$	31.62	MPa
$\nu_{12} = \nu_{13}$	0.35	-	$\eta$	2	-
$\nu_{23}$	0.4	-	$k$	$1 \times 10^5$	N/mm <sup>3</sup>
			$\tau_c$	$1 \times 10^{-3}$	s
			$a_c$	1.	
			$d_{max}$	0.9999	

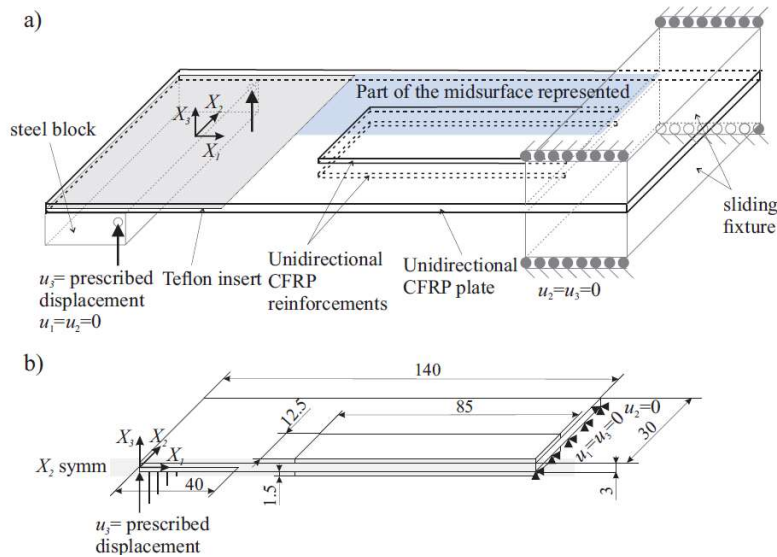


**Figure 3-13: a) Sketch of the partially reinforced ELS specimen. b) Simplified model for FE simulation and dimensions (units in mm)**

### 3.2.2.2. Unsymmetric ELS test

This section describes an unsymmetrical ELS study that serves to validate the implementation of the  $J$ -integral formulation. The reference analysis was performed with Abaqus and the results to be validated were generated with the Samcef solver. This coupon specimen simulation reproduces an ELS test. However, the displacement is only applied to one node at the corner of the notched side of the specimen. In this way, a curved delamination front is promoted. All nodes at the other end of the sample are clamped. The dimensions of the specimen are illustrated in Figure 3-14. The input parameters are listed in Table 3-7. As a way to check the  $J$ -integral implementation, the fracture toughness is set to be mode independent ( $G_c = G_{Ic} = G_{shc} = 0.5$ ) to ensure a constant  $J$ -value (during static crack propagation). Thus, the sum of the three mode-decomposed  $J$ -integrals must be constant and equal to 0.5 at every integration contour, regardless of the loading mode. One quasi-static step is defined: a quasi-static ramp from unloaded to a prescribed displacement of 5.946.

**Table 3-7. Laminate and interface properties for ELS test in section 3.2.2.2**

Laminate properties			Interface properties		
$E_{11}$	150	GPa	$G_{Ic}$	0.5	N/mm
$E_{22} = E_{33}$	10	GPa	$G_{shc}$	0.5	N/mm
$G_{12} = G_{13}$	4	GPa	$\tau_{Io}$	50	MPa
$G_{23}$	2	GPa	$\tau_{sho}$	50	MPa
$\nu_{12} = \nu_{13}$	0.35	-	$\eta$	2	-
$\nu_{23}$	0.4	-	$k$	$1 \times 10^5$	N/mm <sup>3</sup>
$\nu_{23}$	0.4	-			

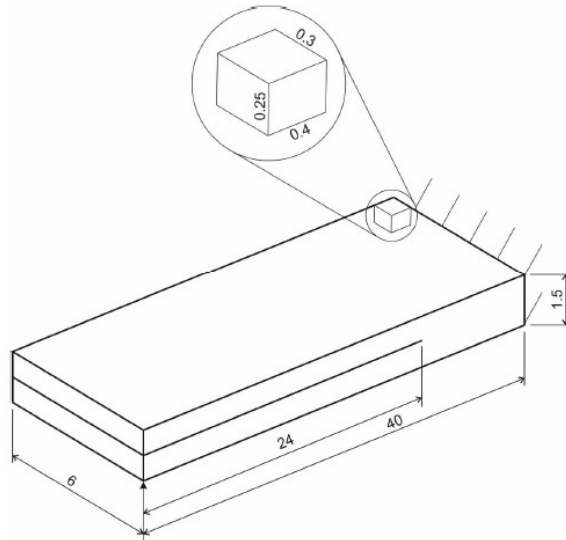


**Figure 3-14: Dimension of the unsymmetric ELS specimen**

### 3.2.2.3. DCB under fatigue loading

In order to validate the implementation of the fatigue damage law in Samcef, a DCB test under fatigue loading is used. The analysis is also performed with Abaqus, as the reference. As shown in Figure 3-15, the coupon specimen is loaded under pure mode I conditions. The fatigue load is applied in two steps:

- A quasi-static ramp from unloaded to a prescribed bending moment of 1050 Nmm
- A fatigue step with a constant maximum cyclic bending moment of 1050 Nmm

The geometry, the boundary conditions and the mesh are represented in Figure 3-15. The moment is applied via shell elements connected to the DCB arms made of solid elements. The macro command .APS is used to connect the shell edge to the surface of the solid structure. All nodes at

the uncracked end of the specimen are clamped. The structure is modeled by hexahedral elements sized 0.3 mm x 0.3 mm x 0.25 mm. The cohesive zone (marked orange) is meshed by zero thickness hexahedral cohesive elements sized 0.3 mm x 0.3 mm. The bulk material is isotropic with a Young's modulus of  $E=2.1\text{e6 MPa}$  and a Poisson's ratio of  $\nu = 0.3$ . The parameters related to the interface law are listed in Table 3-8.

With a pure bending moment applied at the DCB arms, the energy release rate in mode I,  $G_I$ , can be determined analytically based on the  $J$ -integral approach by assuming plane stress conditions:

$$G_I = \frac{12M^2}{Eh^3b^2} = 0.415 \text{ N/mm} \quad \text{Eq. 3-7}$$

where  $h$  and  $b$  are the height and width of each arm, respectively,  $E$  is its Young's Modulus,  $\nu$  is its Poisson's ratio, and  $M$  is the moment applied on each arm of the DCB specimen.

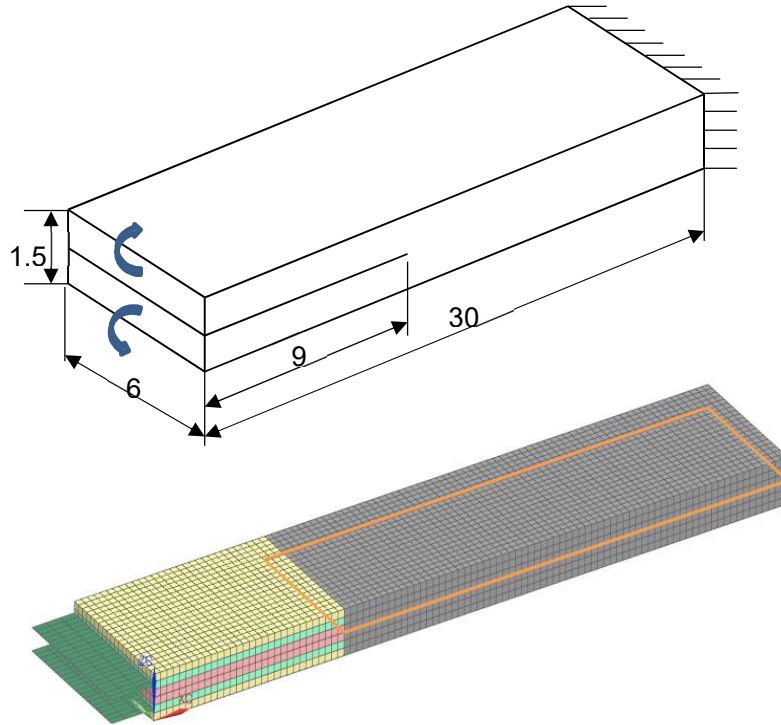


Figure 3-15: Dimensions and FE model of DCB specimen

**Table 3-8.: Interface material properties for DCB test**

Interface properties		
$\mathcal{G}_{Ic}$	1	N/mm
$\mathcal{G}_{sh\ c}$	1	N/mm
$\tau_{Io}$	50	MPa
$\tau_{sh\ o}$	50	MPa
$\eta$	2	-
$k$	$10^5$	N/mm <sup>3</sup>
$\tau_c$	$10^{-3}$	s
$d_{max}$	1.0	-
$A_I$	1	mm/cycle
$A_{sh}$	1	mm/cycle
$A_m$	1	mm/cycle
$p_I$	1	-
$p_{sh}$	1	-
$p_m$	1	-

### 3.2.3. Delamination demonstrator

A validation against the experimental tests GG\_EP\_UD\_002\_DEM\_03 and GG\_EP\_UD\_002\_DEM\_04 presented in Section 3.1.2 is also performed. The geometry and the finite element model are schematized in Figure 3-16. Like in the study case presented in Section 3.2.2.3, the specimen is loaded under pure mode I bending moment. Two simulations under two different loading sequences have been performed. The fatigue load sequence applied in the first simulation case (CASE A) is defined in four steps:

1. A quasi-static ramp from the unloaded state to an applied bending moment of 40 Nm
2. A fatigue step with a constant maximum cyclic bending moment of 40 Nm until 500,000 cycles
3. A quasi-static ramp from an applied bending moment of 40 Nm to 60 Nm
4. A fatigue step with a constant maximum cyclic bending moment of 60 Nm until 800,000 cycles

In the second simulation case (CASE B), the load sequence is defined in two steps:

1. A quasi-static ramp from the unloaded state to an applied bending moment of 40 Nm
2. A fatigue step with a constant maximum cyclic bending moment of 40 Nm until 1,000,000 cycles

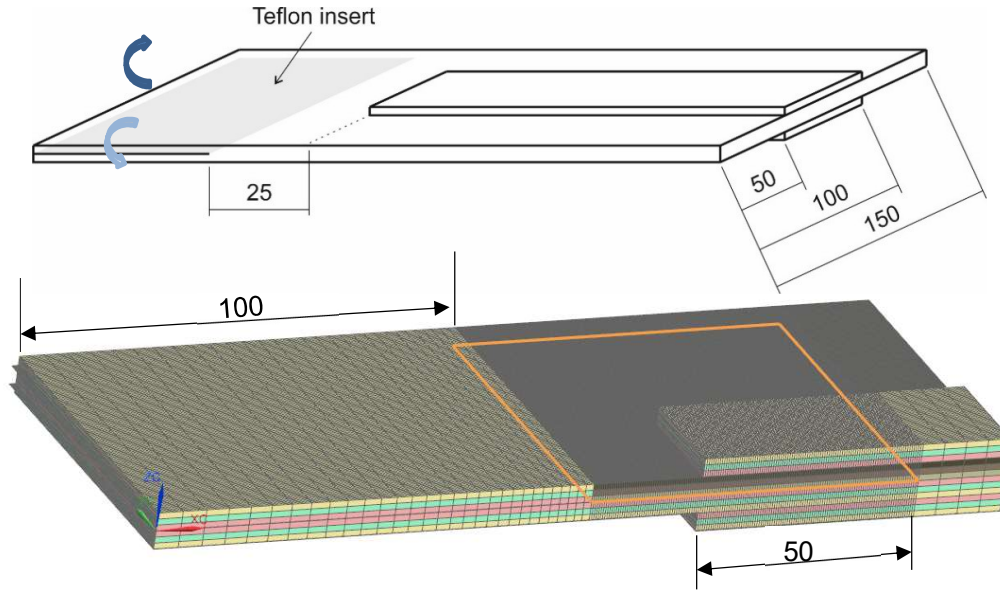


**Figure 3-16: Dimensions and FE model of demonstrator**

For simplicity, only half of the structure is considered and symmetry boundary conditions are applied. The half structure is modeled by hexahedral elements. The cohesive zone (marked in orange) is meshed with zero thickness hexahedral cohesive elements sized 0.5 mm x 0.5 mm. The material properties of the UD ply and the interface are given in Table 3-9.

**Table 3-9.: Ply and interface properties for finite element demonstrator**

Ply properties			Interface properties	
$E_{11}$	37.2	GPa	$\mathcal{G}_{Ic}$	1.359 N/mm
$E_{22}$	15.08	GPa	$\mathcal{G}_{shc}$	5.328 N/mm
$E_{33}$	14.2	GPa	$\tau_{Io}$	20 MPa
$G_{12}$	4.828	GPa	$\tau_{sho}$	40 MPa
$G_{13}$	2.2	GPa	$\eta$	2 -
$G_{23}$	1.5	GPa	$k$	$10^5$ N/mm <sup>3</sup>
$\nu_{12}$	0.308	-	$d_{max}$	1.0 -
$\nu_{13}$	0.25	-	$A_I$	0.1343 mm/cycle
$\nu_{23}$	0.33	-	$A_{sh}$	1 mm/cycle
			$A_m$	1 mm/cycle
			$p_I$	3.984 -
			$p_{sh}$	1 -
			$p_m$	1 -

According to Eq. 3-7, the analytical value for the energy release rate in mode I at the initiation of the test with a straight crack front is  $\mathcal{G}_I = 0.31$  N/mm.

## 4. Results and discussion

### 4.1. Characterization testing

In order to obtain the flexural modulus, ( $E$  in Eq. 3-2) to calculate the energy release rate for the data reduction of the following tests, three-point bending tests were performed to the seven specimens listed in Table 4-1.

**Table 4-1. Flexural modulus obtained from three-point bending tests**

Specimen identification	$E_f$ (MPa)
0-0 B1000 F 11	37846.94
0-0 B1000 E 04	35496.33
0-0 B1000 F 08	36265.31
0-0 B1000 E 03	37908.46
0-0 B1000 E 01	37870.40
0-0 B1000 F 16	38947.61
0-0 B1000 F 17	36093.39
<b>Average</b>	<b>37204.06</b>

#### 4.1.1. Quasi-static properties

Quasi-static fracture toughness tests were performed following the method specified in Section 3.1.1. A batch of six DCB coupon specimens were tested. Measurements of the specimen thickness and width were taken at the specified measurement points (see Figure 4-1). The average width and thickness are listed in Table 4-2. All specimens were 657 mm long and the initial crack length from the tab was 75 mm. A pre-rotation of  $-7.5^\circ$  and  $7.5^\circ$  was applied at the upper and lower moment arms, respectively, to compensate for the moment arms rotation at the end of the test. The horizontal distance between the two points of load application,  $s$ , at the unloaded configuration was 167 mm (corresponding to the rollers placed at the 1<sup>st</sup> and 7<sup>th</sup> holes of the moment arms).

**Table 4-2. Identification and dimensions (in mm) of the DCB coupon specimens tested for measuring the mode I fracture toughness,  $G_{Ic}$**

Specimen identification	Height (micromet. $\pm 0.01$ )	Width (calliper $\pm 0.1$ )
0-0 B1000 C 01	12.15	27.78
0-0 B1000 C 02	12.30	27.76
0-0 B1000 C 03	12.15	27.84
0-0 B1000 C 04	12.10	27.62
0-0 B1000 C 05	12.18	28.11
0-0 B1000 C 06	12.22	27.77

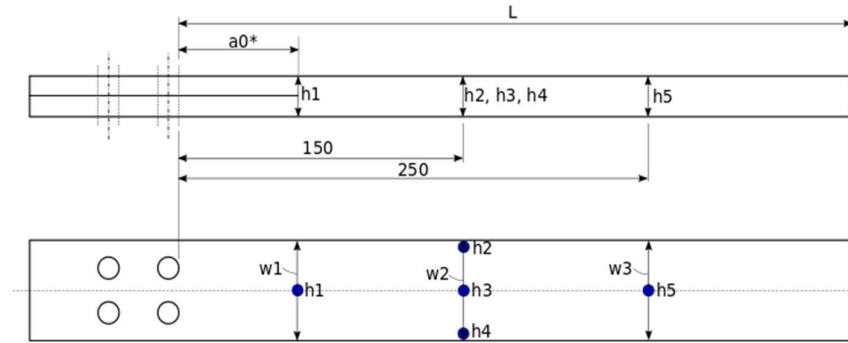


**Figure 4-1. Specimen dimensions measurement points**

The measured mode I energy release vs load point rotation results are shown in Figure 4-2. The average flexural modulus  $E = 37.2$  GPa listed in Table 4-1 was used in Eq. 3-2 for the calculation of the energy release rate. The data set for each specimen listed in Table 4-2 is plotted on the left, while the average, minimum and maximum curves for the combined data sets are plotted on the right. The propagation fracture toughness,  $G_{Ic}$ , obtained by integration of the average curve divided by the span load point rotation in the steady propagation region (plateau) is  $1359 \text{ J/m}^2$ .

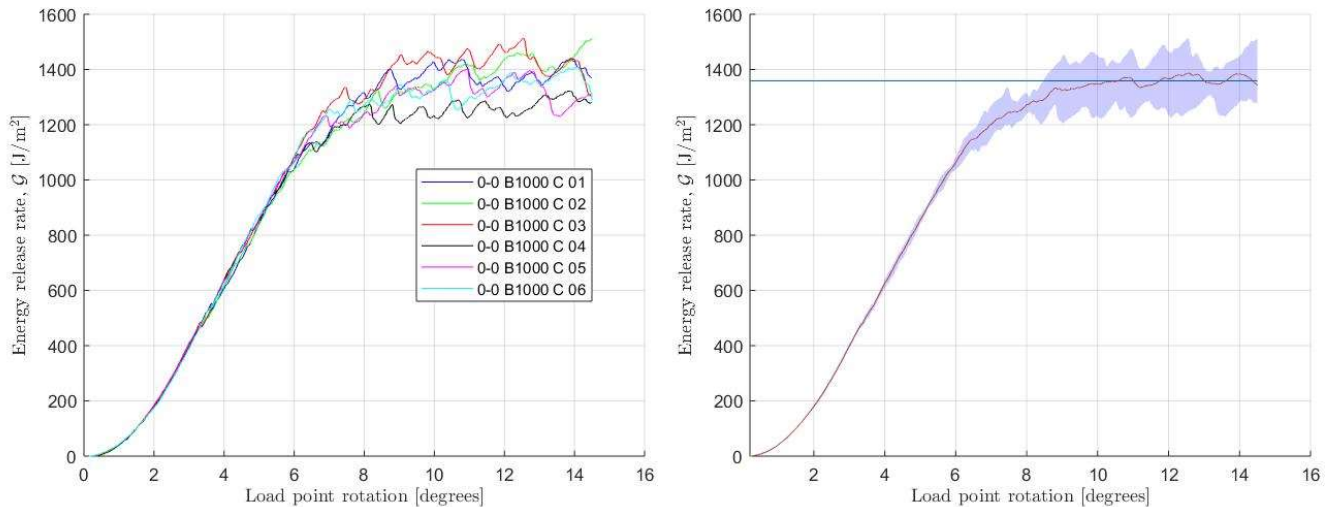


**Figure 4-2. Mode I energy release rate vs the load point rotation for the individual data set corresponding to different specimens (left) and the averaged, maximum and minimum curves (right). The propagation fracture toughness,  $G_{Ic}$ , value is represented with a blue solid horizontal line (right).**

#### 4.1.2. Fatigue properties

Crack growth rate tests under fatigue loading conditions were performed following the method specified in Section 3.1.1. A batch of five DCB coupon specimens were tested. Measurements of the specimen thickness and width were taken at the specified measurement points (see Figure 4-1). The average width and thickness are listed in Table 4-3. All specimens were 657 mm long and the initial crack length from the tab was 75 mm.

**Table 4-3. Identification and dimensions (in mm) of the DCB coupon specimens tested for measuring the mode I fracture toughness,  $A_i$ ,  $p_i$ .**

Specimen identification	Height (micromet. $\pm 0.01$ )	Width (calliper $\pm 0.1$ )
0-0 B1000 E 01	12.18	27.78
0-0 B1000 E 04	12.27	27.76
0-0 B1000 F 11	12.20	27.84
0-0 B1000 F 16	12.00	27.62
0-0 B1000 F 17	12.28	28.11

The crack growth rate  $da/dN$  is plotted against the energy release rate  $\mathcal{G}$  for the five specimens in Figure 4-3. In this case, the corresponding flexural modulus for each specimen (listed in Table 4-1) was used in Eq. 3-2 for the calculation of the fracture toughness. It was chosen to fit a crack growth rate model to the combined data set and not to each specimen dataset since the differences between the datasets were relatively large. The used crack growth rate model is a power law on the form  $da/dN = C \cdot \mathcal{G}^m$ . This model was fitted to the combined data using a weighted linear least squares criterion on a linearized version of the original power law given by  $\log(da/dN) = \log(C) + m \cdot \log(\mathcal{G})$ . It is worth noting that the data sets were not showing a log-linear trend for the entire  $\mathcal{G}$  range explored during the fatigue tests. Thus, the fitting of a Paris' law-like expression did not match the dataset for the entire  $\mathcal{G}$  range. In order to overcome this situation, the data sets were cropped to the applied  $\mathcal{G}$  range in the demonstrator tests presented in Section 4.2. The crack growth rate  $da/dN$  was used as weight. The weighted least squares fit was obtained by minimizing the following expression with  $\log(C)$  and  $m$  as the parameters to be determined.

$$\sum_{i=1}^n (da/dN)_i \cdot (\log_{10}(da/dN)_i - \log_{10}(C) + m \cdot \log(\mathcal{G})_i)^2 \quad \text{Eq. 4-1}$$

The spacing between data points in terms of the energy release rate  $\mathcal{G}$  was varying throughout the test in the sense that the spacing was large for large  $\mathcal{G}$  and vice versa. In order not to let the spacing between data points bias the fit of the crack growth rate model in an uncontrolled manner, each dataset was linearly interpolated with evenly spaced energy release rate values before the fit was done. The same values of  $\mathcal{G}$  were used for the interpolated values for all the datasets. The increment in  $\mathcal{G}$  for the interpolated datasets was set to 0.1 J/m<sup>2</sup>. The fitting of the combined data set led to the following Paris' law-based equation:

$$da/dN = 1.6374e - 13 \cdot \mathcal{G}^{3.753} \quad \text{Eq. 4-2}$$



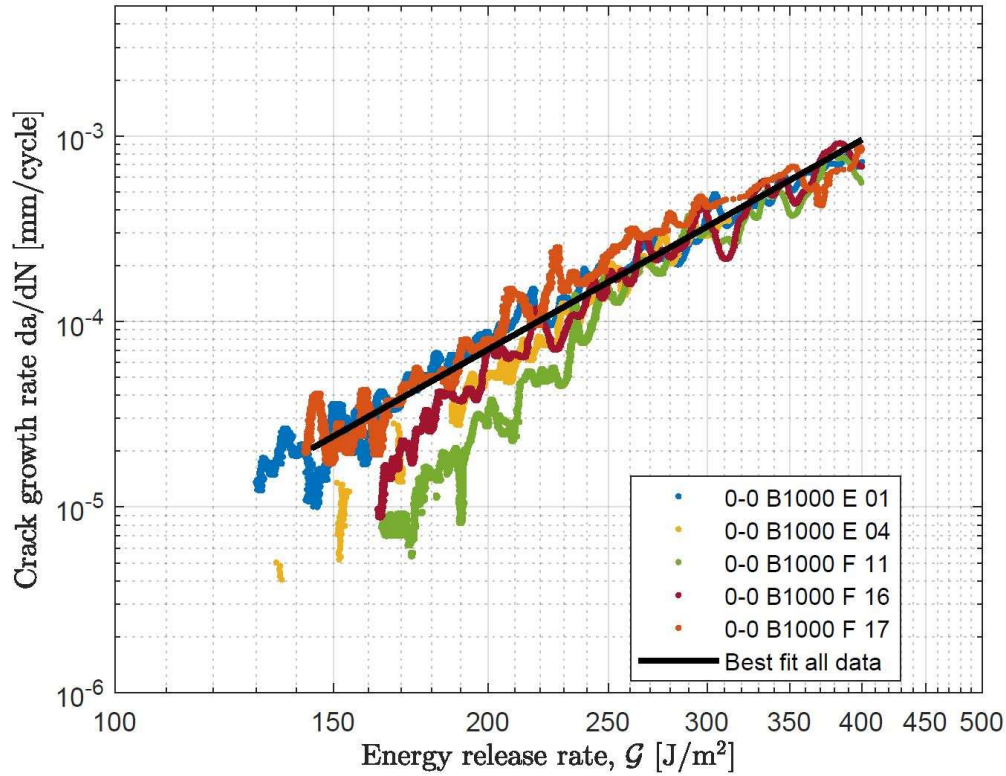


**Figure 4-3. Crack growth rate vs energy release rate. Data has been cropped to the applied  $G$  range in the demonstrator tests presented in Section 4.2.**

Taking into account that tests were performed at a load ratio  $R = 0.1$  and the measured mode I fracture toughness  $G_{Ic} = 1359 \text{ J/m}^2$  (see Section 4.1.1), Eq. 2-14 can be expressed as:

$$\frac{da}{dN} = \begin{cases} 0.1396 \left( \frac{G_{max} (1 - 0.1)}{1359} \right)^{3.753} & \text{for } 0 < G_{max} < 1359 \\ 0 & \text{for } G_{max} \leq 0 \end{cases} \quad \text{Eq. 4-3}$$

Since the data sets were cropped to the applied  $G$  range in the demonstrator tests presented in Section 4.2, the threshold was not characterized, and it was set to 0 in Eq. 4-3.

## **4.2. Delamination demonstrator – A comparison between testing and simulation results**

### **4.2.1 Testing results of the delamination demonstrator**

Fatigue tests were performed following the method specified in Section 3.1.2. A batch of four demonstrator specimens were tested. The load sequence in terms of applied moment and number of fatigue cycles is listed in Table 4-4 for every test specimen. The two first tests consist of one single load step, meaning that the applied moment was constant during the entire test. The two last tests consist of two load steps meaning that the applied moment was changed to a higher load level after a certain number of cycles. This was done because the crack propagation arrested at the reinforcement edge due to stiffening effect of the reinforcement. Thus, in order to promote further crack propagation, the applied moment was increased after a certain number of cycles during which the crack front was propagating very slowly.

**Table 4-4. Load sequence of the fatigue tests performed on the demonstrator specimens**

Specimen ID	Number of load steps	Applied moment (Nm)	Number of cycles
GG_EP_UD_002_DEM_01	1	65	122,115
GG_EP_UD_002_DEM_02	1	50	329,464
GG_EP_UD_002_DEM_03	2	40	475,356
		60	202,533
GG_EP_UD_002_DEM_04	2	40	475,585
		60	251,663

The test GG\_EP\_UD\_002\_DEM\_01 showed static propagation at the first cycle. Thus, the crack front propagated statically and stopped at the reinforcement edge (see Figure 4-4). From that point, fatigue propagation occurred due to applied cyclic loading. However, after the test was finished and the specimen was removed from the testing rig, the lower reinforcement was visibly debonded from the plate. It is assumed that the bondline failure occurred during the static propagation, making the specimen dissimilar with respect to the midplane and thus pure mode I loading cannot be assumed at the crack tip during the fatigue test. Thus, this test is considered invalid.

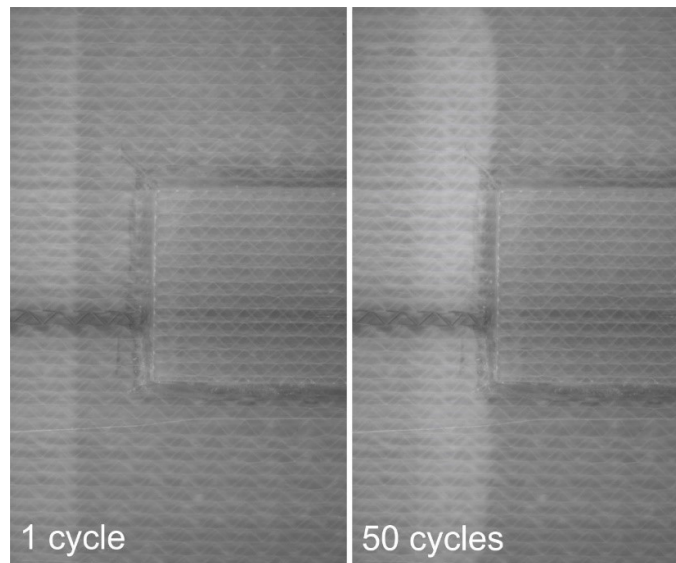


**Figure 4-4. The crack front propagated statically during the first cycle in test GG\_EP\_UD\_002\_DEM\_01. Note that the picture acquisition frequency during this test was set to one picture every 50 cycles. Thus, the first picture available is after 50 cycles.**

The crack front evolution at selected number of cycles during the tests GG\_EP\_UD\_002\_DEM\_02, GG\_EP\_UD\_002\_DEM\_03 and GG\_EP\_UD\_002\_DEM\_04 are shown in Figure 4-5, Figure 4-6 and Figure 4-7, respectively. Note that tests EP\_UD\_002\_DEM\_03 and GG\_EP\_UD\_002\_DEM\_04 were designed identical to check the repeatability of the results. It can be concluded that both tests show a similar evolution of the crack front in terms of both shape and propagation rate. The location of the crack front in both tests is quite coincident at the selected number of cycles shown Figure 4-6 and Figure 4-7.

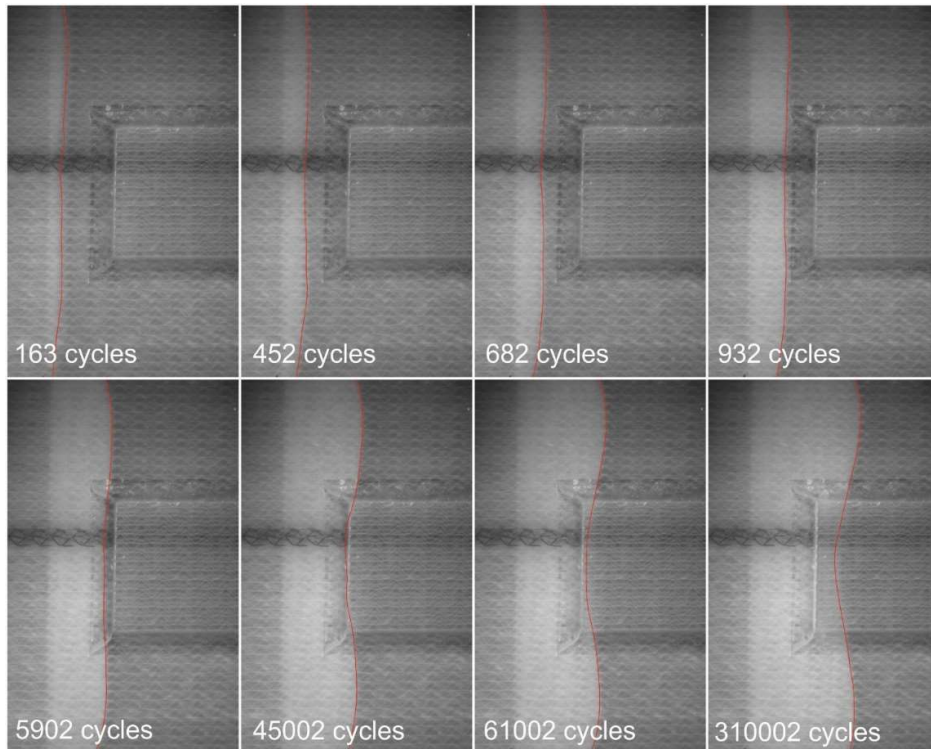


**Figure 4-5. Crack front evolution during the test GG\_EP\_UD\_002\_DEM\_02. The crack tip location is highlighted in red.**

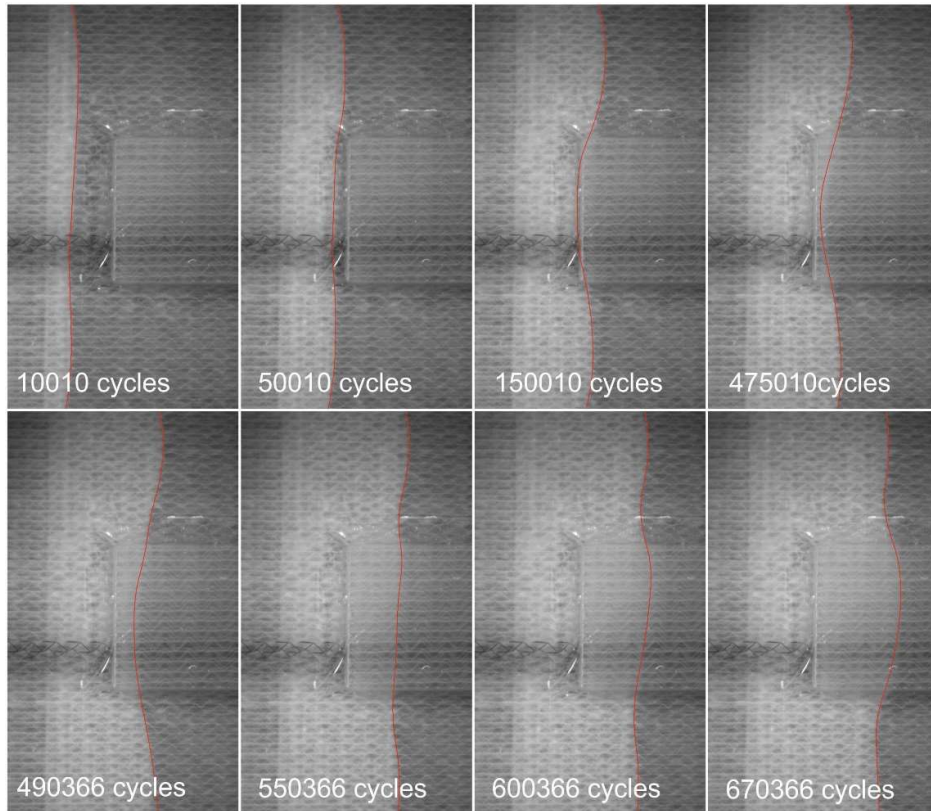


**Figure 4-6. Crack front evolution during the test GG\_EP\_UD\_002\_DEM\_03. The crack tip location is highlighted in red.**

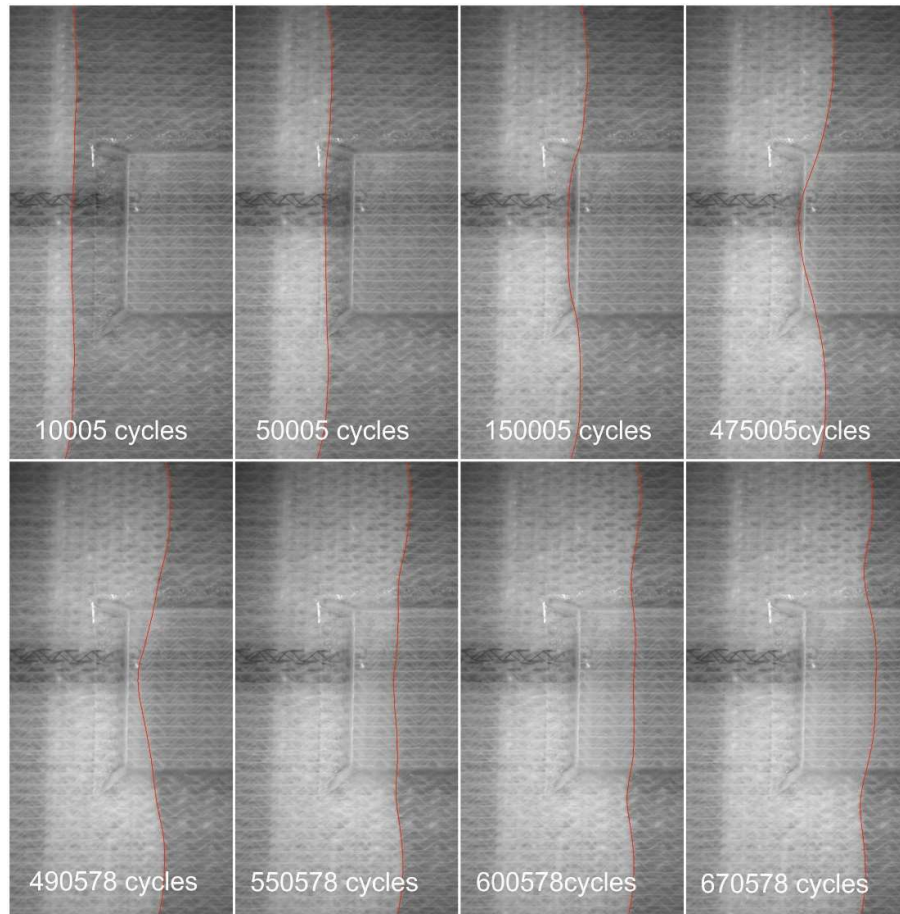


**Figure 4-7. Crack front evolution during the test GG\_EP\_UD\_002\_DEM\_04. The crack tip location is highlighted in red.**

## 4.2.2 Simulation results of the implementation validation cases

### 4.2.2.1. Reinforced ELS test

Figure 4-8 shows the evolution of force with respect to the prescribed displacement for the simulation done with Samcef and Abaqus, as the reference solver. The stiffness and the maximum load are in agreement, which validates the implementation of the quasi-static cohesive law. The discrepancy in both results after the maximum force peak can be explained by a different maximum damage,  $d_{max}$ , and the difference of cohesive viscous effect parameters,  $\tau_c$  and  $a_c$ .



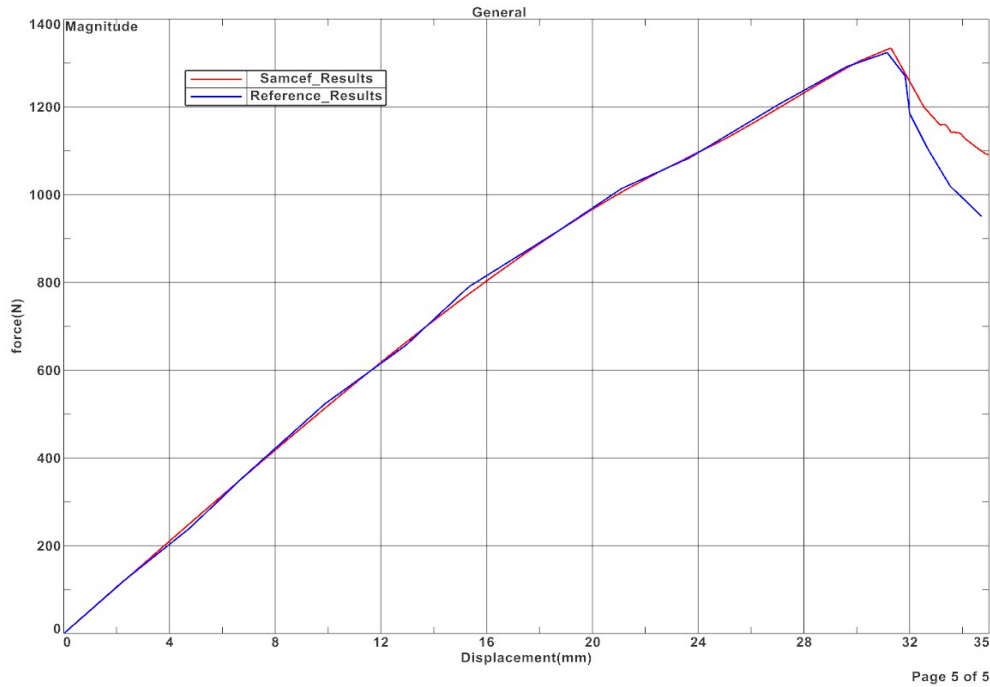


**Figure 4-8: Evolution of force in respect displacement for ELS simulation**

Figure 4-9 shows the distribution of the angle between GDD and the local coordinate,  $e_1$  (see Figure 2-2) at the specimen midplane. Note that, as shown in Figure 3-13, only half of the specimen is represented, since it shows symmetry with respect to the coordinate  $X_2$ . The angle is equivalent with a shift of 180 degree. This is because the local coordinate  $e_1$  is oriented in opposite direction in the respective analysis in Samcef and Abaqus.

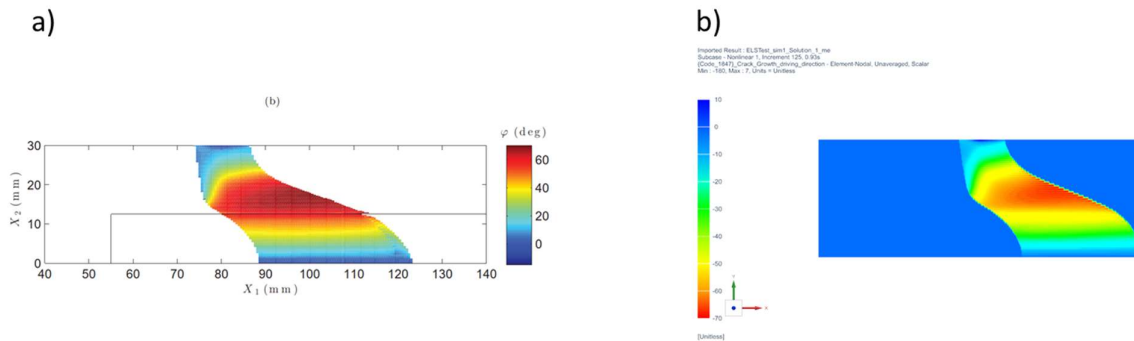


**Figure 4-9: Field of angle between GDD in local frame with a) Abaqus and b) Samcef solver**

#### 4.2.2.2. Unsymmetric ELS test

Figure 4-10 and Figure 4-11 show the  $J$ -integral components obtained from the simulations in Abaqus (reference) and Samcef solver, respectively. The sum of the  $J$ -integral components is equivalent to  $G_c$ , as expected since the cracks propagate in static manner. Figure 4-12 and Figure 4-13 show the energy-based damage and the GDD obtained from the simulations in Abaqus (reference) and Samcef solver, respectively. The results are equivalent, which validates the implementation in Samcef.

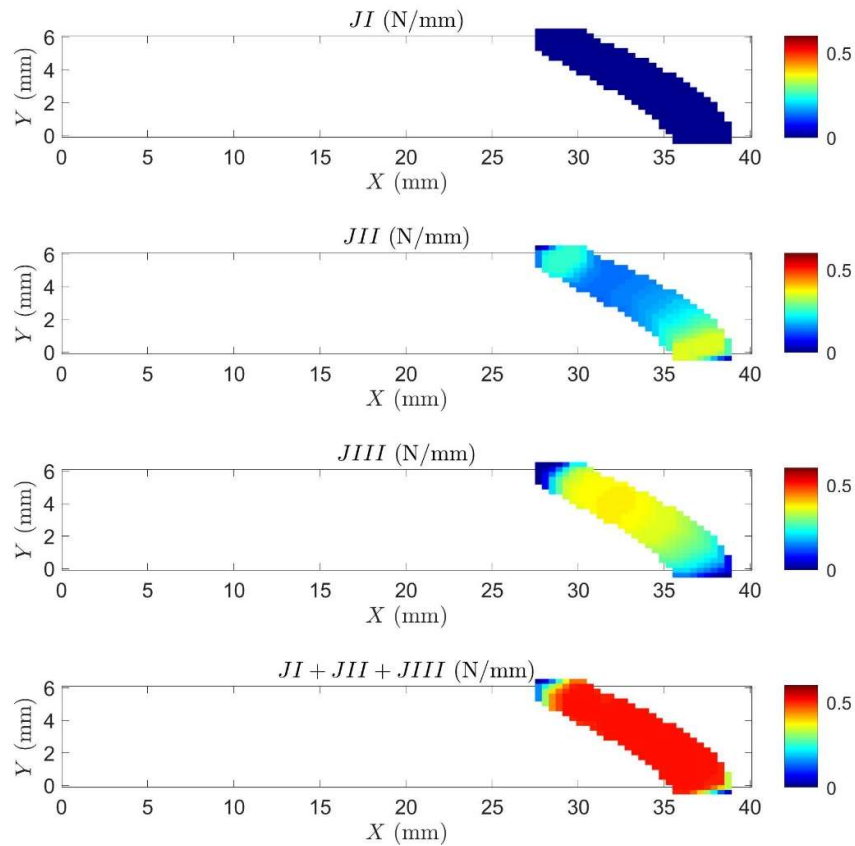


Figure 4-10: Distributions of mode I (top-right), mode II (down-left) and mode III (down-right) components of the J-integral obtained from the simulation with Abaqus (reference).

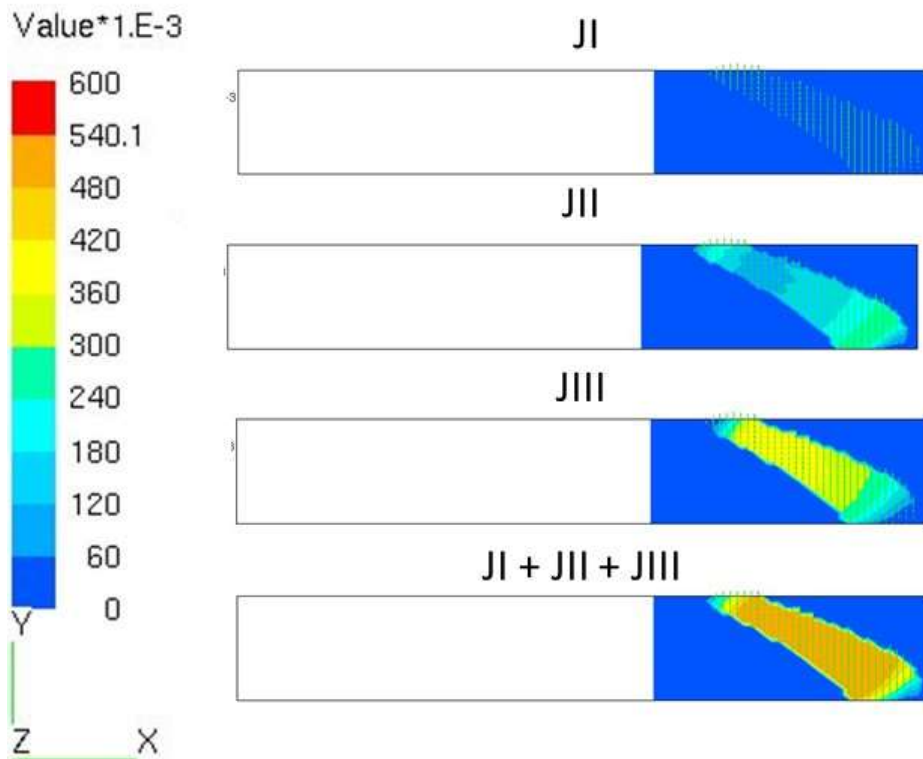
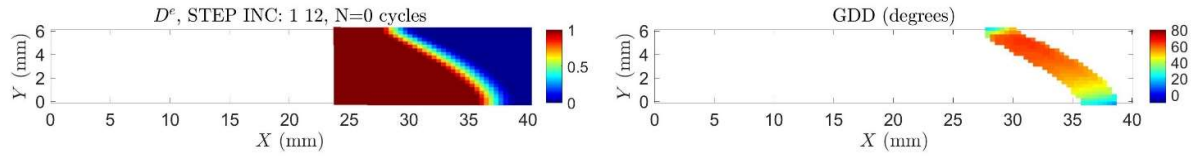
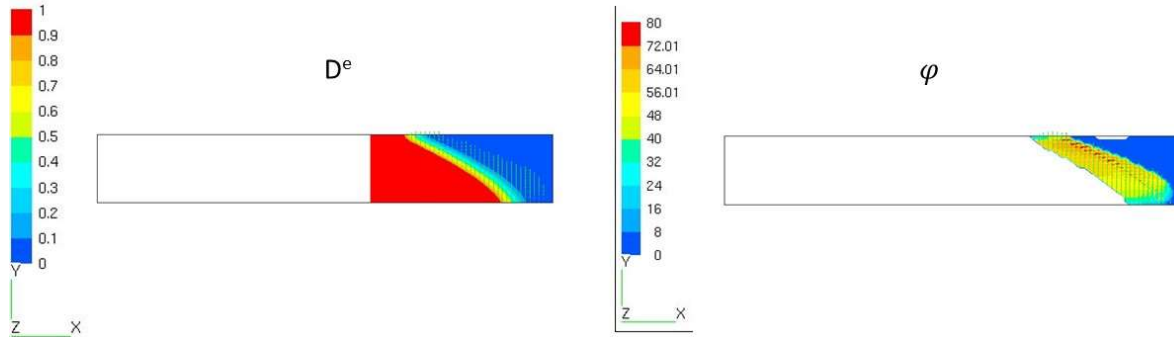


Figure 4-11: Distributions of mode I, mode II, mode III (down-right) components and sum of the J-integral obtained from the simulation with Samcef



**Figure 4-12: Distribution of energy-based damage (top-left), GDD (top-right), mode mixity (down-left) and  $J$ -integral (down-right) obtained from the simulations with Abaqus (reference).**



**Figure 4-13: Field of energy-based damage and GDD from the simulation with Samcef.**

#### 4.2.3 DCB Fatigue test

The deformed structure at the end of static step is shown in Figure 4-14. Other results such as energy-base damage  $D_e$ , the GDD, the mode I interlaminar stress,  $\tau_I$ , and the mode  $J$ -integral component,  $J_I$ , at the end of static step and after 35 fatigue cycles are plotted in Figure 4-15 and Figure 4-16, where the reference results generated with Abaqus are also shown for the sake of comparison. The evolution of the number of delaminated elements ( $N_{Del}$ ) at the middle width with the number of cycles is plotted in Figure 4-17.

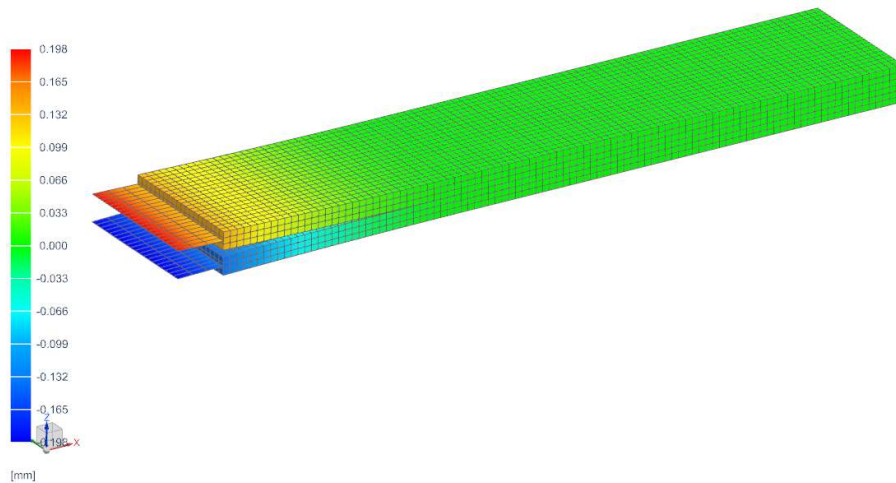
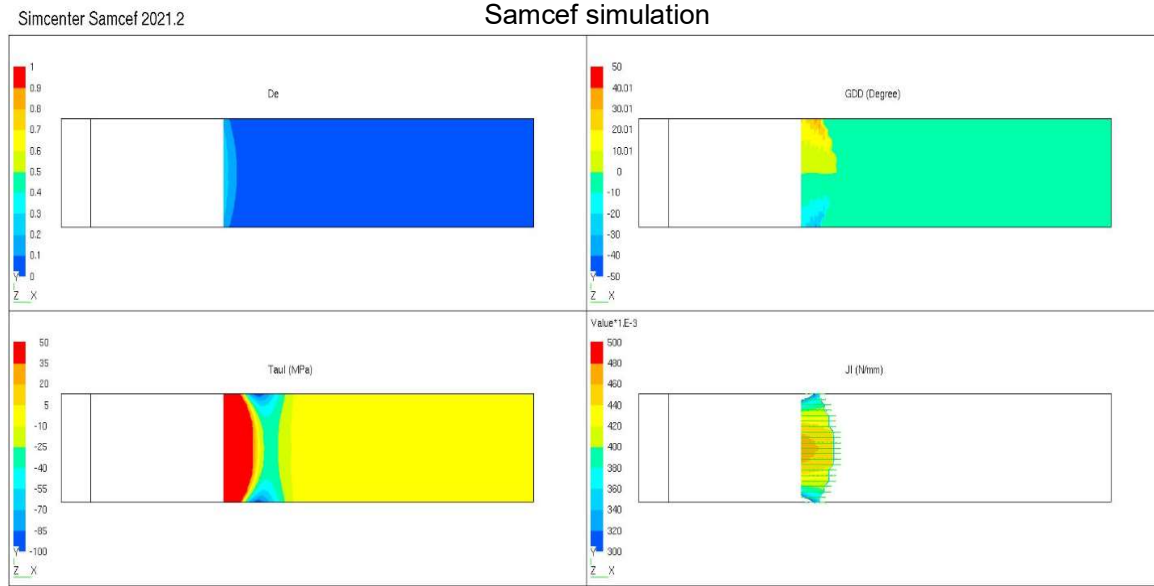


**Figure 4-14: Deformed DCB (U3) at the end of static step**



### Reference

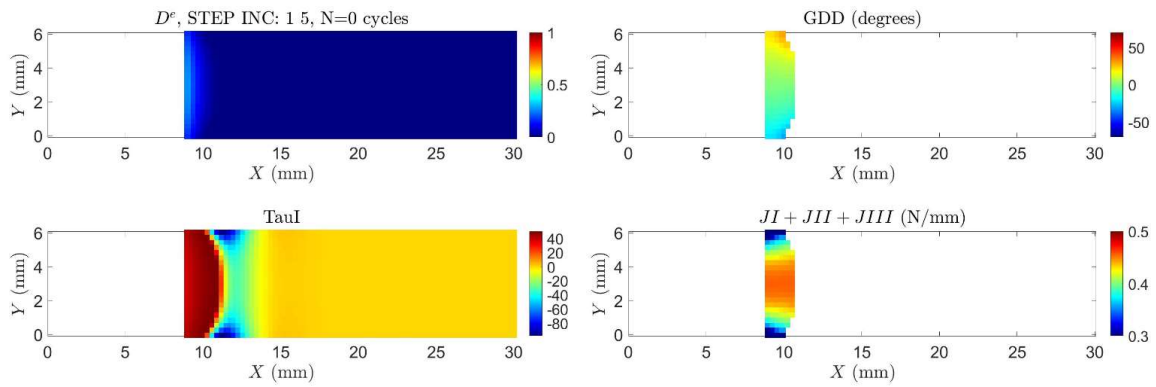
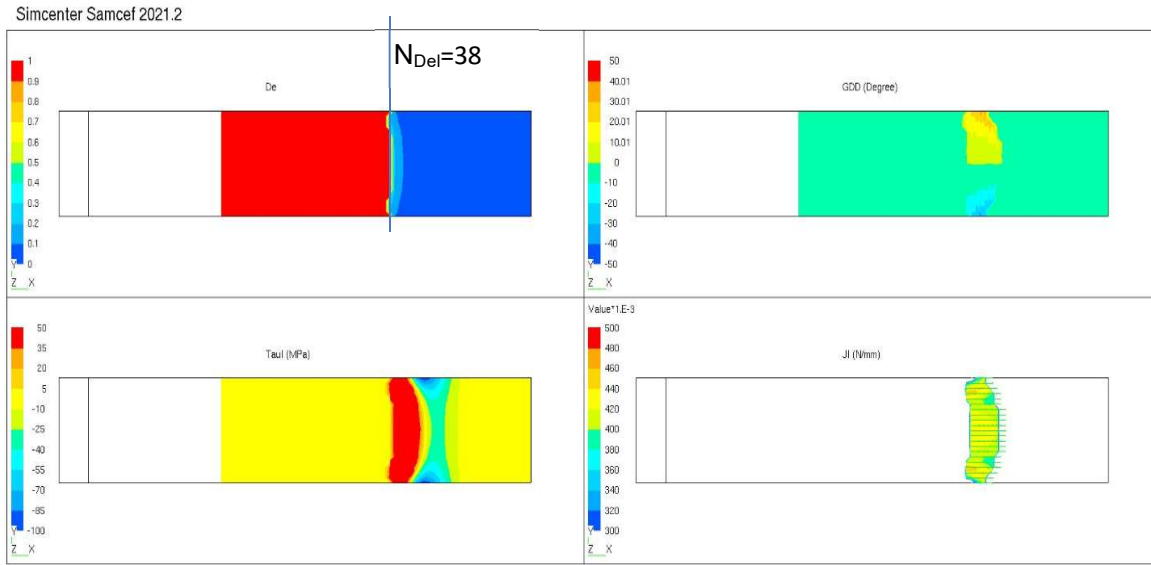


**Figure 4-15: Comparison of the results at the end of static step**



## Samcef simulation



## Reference

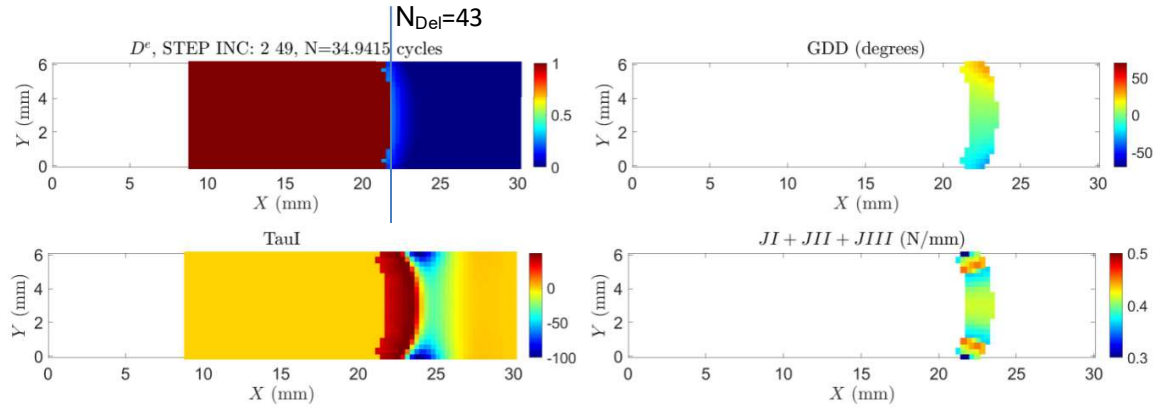
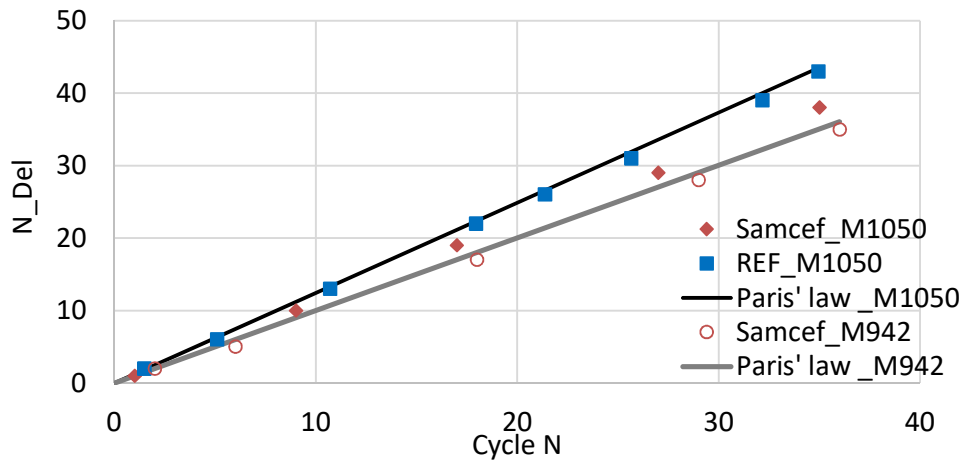


Figure 4-16: Comparison of the results at 35 cycles

Figure 4-17: Evolution of crack growth level ( $N_{Del}$ ) versus cycle (N)

In this case, the evolution of GDD and  $J$ -integral determined with the implemented fatigue model in Samcef is in good agreement with that of the reference. However, the model implemented in Samcef predicts slower crack propagation. The reason is due to the cycle jump strategy. In the reference model, each cycle jump can be determined and precisely executed based on the target crack growth increment  $\Delta a = 0.3$  mm, equivalent to the length of the cohesive element, divided by the maximum crack growth rate in the model. The cycle jump is exactly equal to this ratio, even when the result is a decimal number. Conversely, the cycle jump strategy used in Samcef is based on a statistical analysis. Moreover, the cycle jump is rounded to an integer. Thus, the minimum cycle jump is 1. In the case study, the cycle jump in the reference model was 0.73 cycles, while in the model implemented in Samcef was forced to be equal to 1. In order, to assess the effect of the rounding of the cycle jump, another simulation by changing the applied moment from 1040 Nmm to 942 Nmm, which corresponds exactly the crack growth rate 1 element per cycle, has been performed. Its crack growth level evolution is also plotted in Figure 4-16. In this case, good agreement is observed compared to the solution given by the integration of the Paris' law.

It is also worth mentioning that, in the reference model, as only the maximum envelope load is modeled, the counting of cycles is exactly equal to the accumulated cycle jumps. However, this is not the case in the implementation in Samcef. As show in Figure 4-18, during step 1, an entire fatigue cycle is simulated. Then the first cycle jump is executed, and the total number of fatigue cycles elapsed is  $N_{\text{jump}1} = N_{\text{jump}1} + 1$ , which corresponds to the  $(N_{\text{jump}1} + 1)^{\text{th}}$  cycle. Then, the second, third... and the  $i^{\text{th}}$  cycle jumps follow. The total number of cycles elapsed at the  $i^{\text{th}}$  cycle jump is  $N_{\text{jump}i} = N_{\text{jump}i-1} + N_{\text{jump}i} + 1$ , which corresponds to the cycle  $(\sum_1^i N_{\text{jump}i} + 1)^{\text{th}}$  cycle. Since only the maximum load envelop is modeled in the present fatigue model, the damage during the simulation of the fatigue cycles is kept constant. This leads to an underestimation of the damage variable, which has a notable influence for low-cycle fatigue simulation, but it decreases as the number of cycles of the simulation increases.

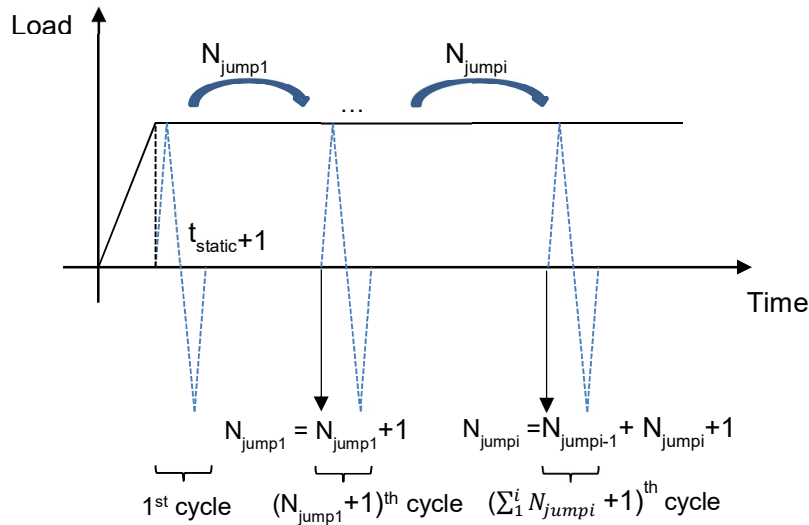
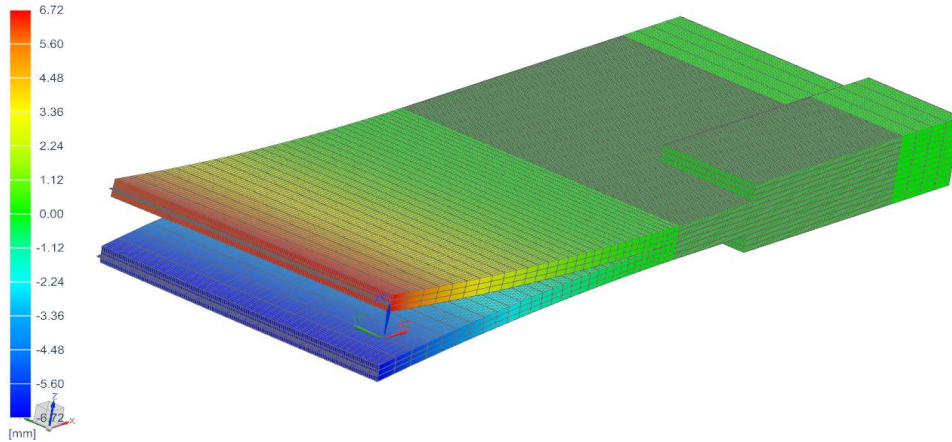


Figure 4-18: Interlaminar fatigue damage analysis in Samcef

#### 4.2.4 Comparison of results on the demonstrator specimen

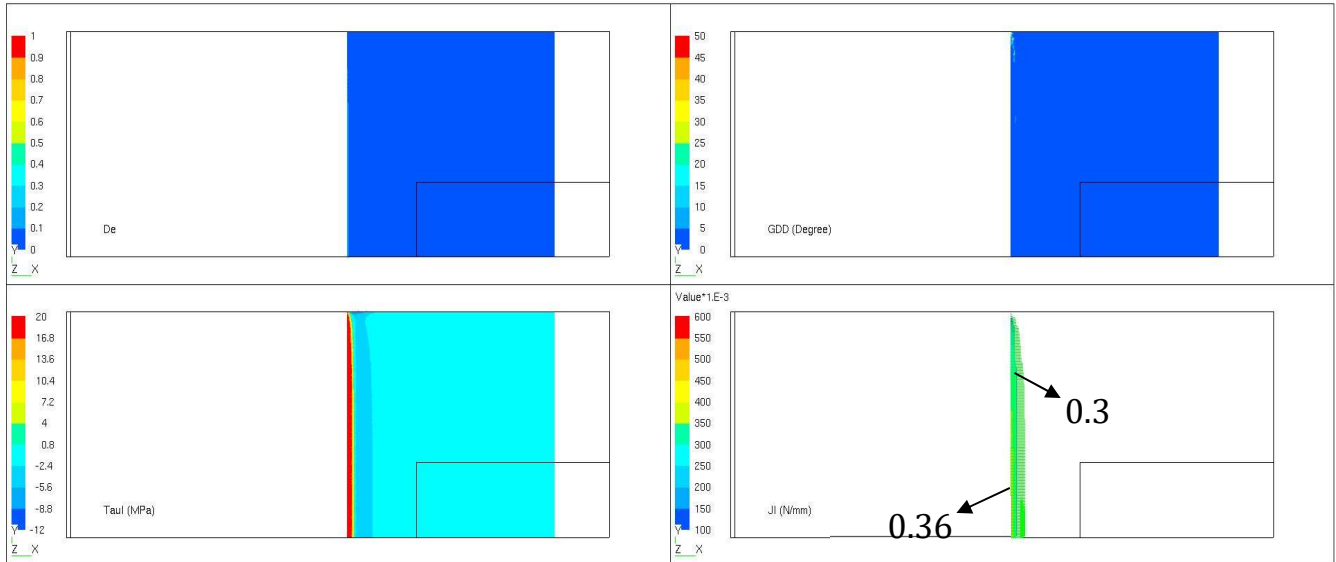
The deformed structure after the static step (step 1 of the simulations cases A and B presented in Section 3.2.3) is shown in Figure 4-19. Other results such as the energy-base damage  $D_e$ , the GDD, the mode I interlaminar stress,  $\tau_I$ , and the  $J$ -integral,  $J_I$ , are shown in Figure 4-20.



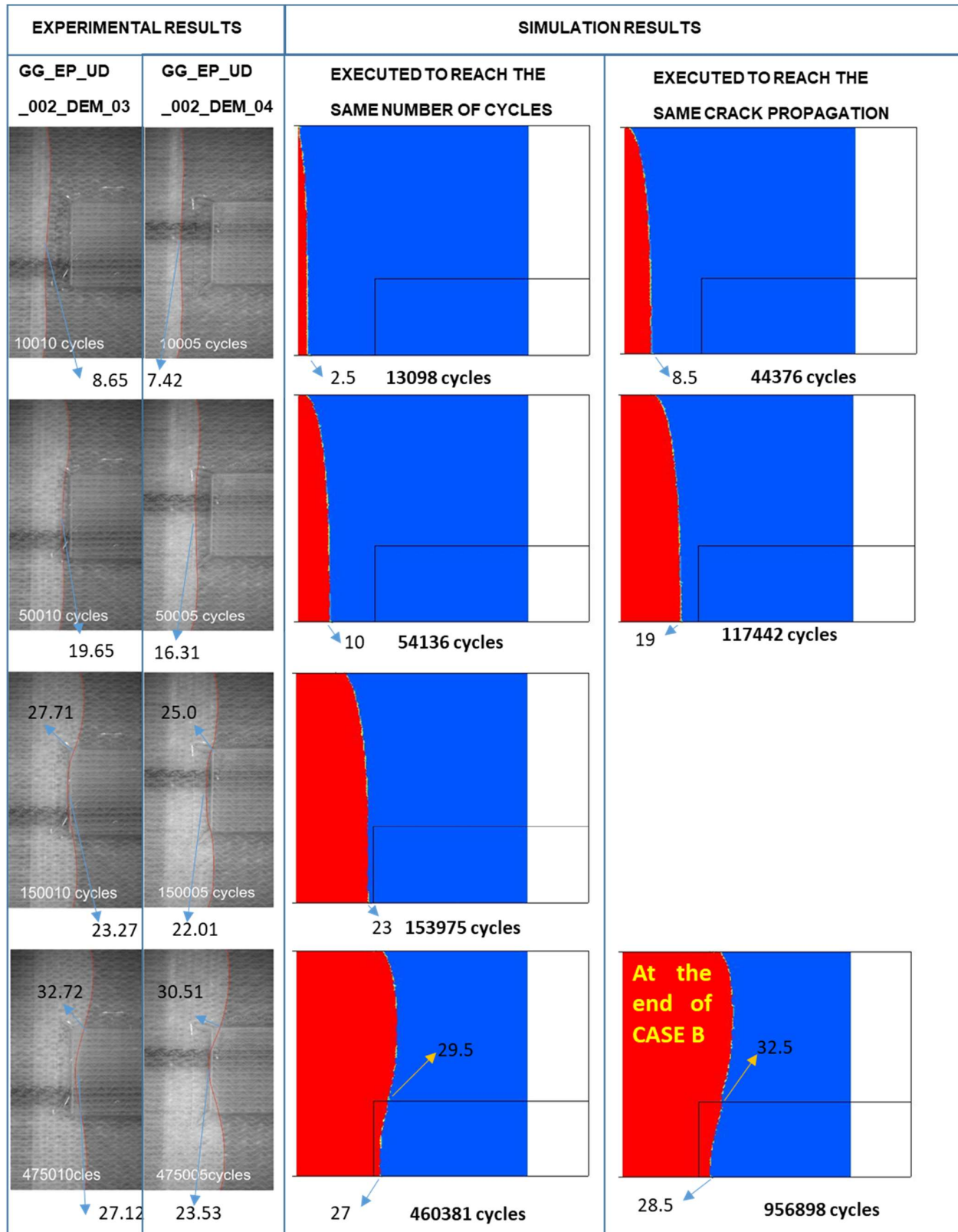
**Figure 4-19: Deformed demonstrator (U3) at the end of static step**

Figure 4-21 shows the evolution of the delamination front position during fatigue analysis with an applied bending moment of 40 Nm (step 2 of the simulations cases A and B presented in Section 3.2.3). Compared to the experimental results (see tests GG\_EP\_UD\_002\_DEM\_03 and GG\_EP\_UD\_002\_DEM\_04 in Section 4.2.1), the simulation results reveal slower crack growth. The maximum difference in crack front position between experimental and simulation results at the different selected number of cycles shown in Figure 4-21 is around 6 mm (after 10k and 50k cycles). At the end of step 2 of CASE A, the difference between experimental and simulation results is around 3 mm. In order to compute the number of cycles required to reach the same crack propagation at the end of step 2, CASE B runs up until 1M cycles. In this case, the delamination propagation from the simulation is delayed with respect to the experimental results by a factor of 2 in the number of cycles. The inhomogeneity of the  $J$ -integral, the cycle jump strategy as explained previously, and even the dispersion of the data from calibration process (see Figure 4-3), could be the reason for this underestimation. However, it is worth mentioning that at the end of step 2, crack propagation is almost arrested due to the stiffening caused by the reinforcements. That is, when the crack front reaches the reinforcement edges, the  $J$ -value decreases due to the increased stiffness. Consequently, the propagation rate also decreases drastically. Due to a very low crack growth rate, a high number of cycles is required to propagate the 2 mm that differs from the experimental results.

Simcenter Samcef 2021.2



**Figure 4-20: Results at the end of static step: energy-based damage (top-left), GDD (top-right), mode I interlaminar stress  $\tau_I$  (down-left) and mode I component of  $J$ -integral (down-right)**



**Figure 4-21: Comparison of numerical and experimental results for delamination front position (mm) with an applied bending moment of 40 Nm (step 2). In order to ease the reading and interpretation of the results, the X coordinate at which the crack front is located is marked with an arrow at selected points.**

Figure 4-22 shows the evolution of the delamination front position during fatigue analysis with an applied bending moment of 60 Nm (step 4 of the simulation case A presented in Section 3.2.3). Compared to the experimental results (see tests GG\_EP\_UD\_002\_DEM\_03 and GG\_EP\_UD\_002\_DEM\_04 in Section 4.2.1), the simulation results reveal again slower crack growth. The difference at the end of the analysis (after 670k cycles) the numerical predictions match the GG\_EP\_UD\_002\_DEM\_04 experimental test results, while the difference with the GG\_EP\_UD\_002\_DEM\_03 experimental test results is less than 7. In order to get similar crack front propagation, the simulation requires extra 85k cycles. In this case, there is no crack arrest and, thus, the number of cycles required to extend the crack by 7 mm is not as high as at the end of step 2.

The GDD and the mode I component of the  $J$ -integral are plotted in Figure 4-23 and Figure 4-24. The simulation method implemented in Samcef successfully reproduces the delamination front shape, which changes its shape from straight to curved due to the reinforcements. It can be visually inspected that the values for the GDD correspond to the angle of the normal to the delamination front with the global x-axis. Before the crack front reaches the reinforced region, the computed  $J$ -integral keeps approximately equal to the analytical value 0.31 N/mm. After the increase of the applied moment during the static loading step 3, the curvature of the crack front is again very well captured. The  $J$ -integral increases due to increased bending moment and in the reinforced region, its value becomes more and more dominant. Consequently, the crack propagates further at the center of the test specimen.

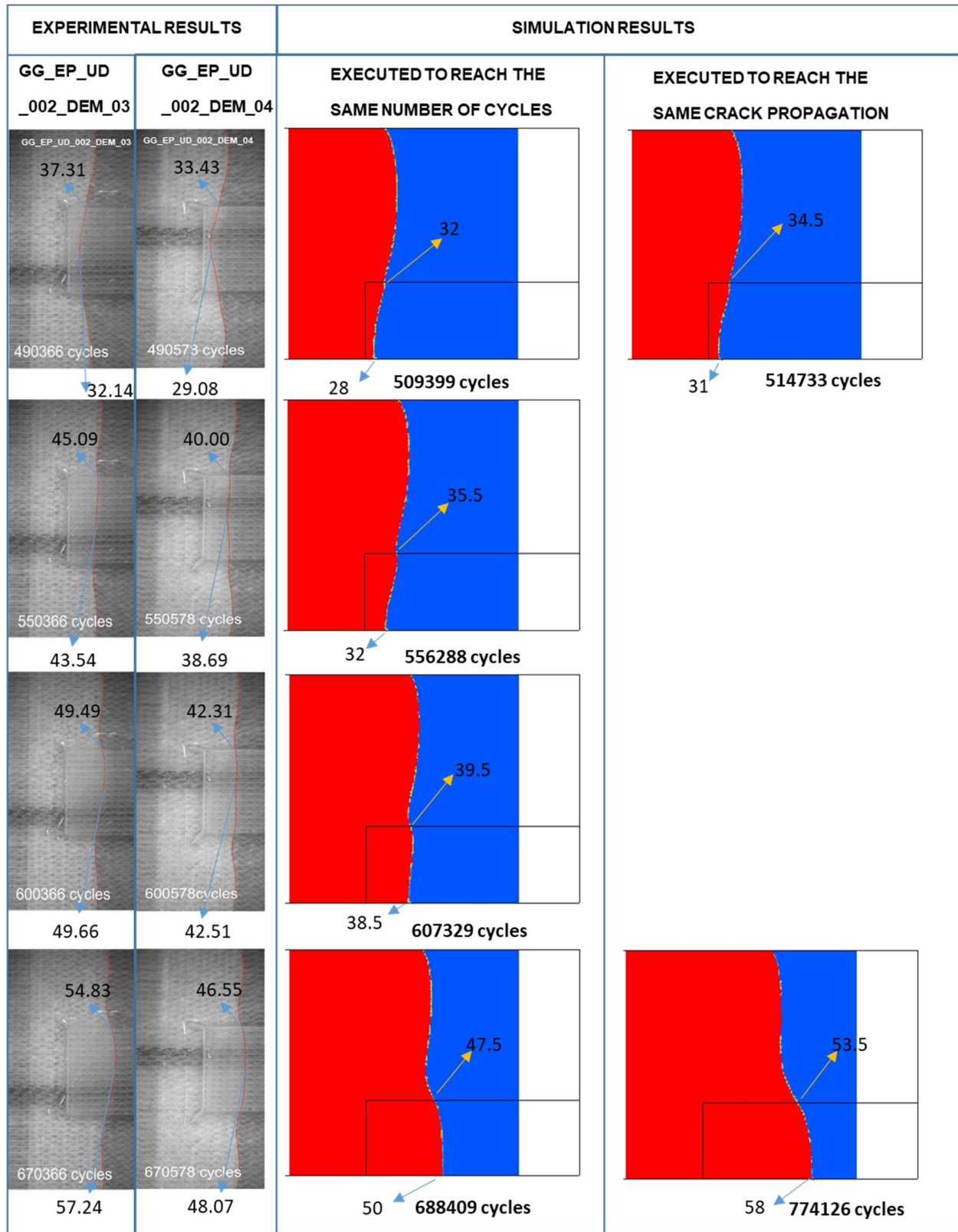


**Figure 4-22: Comparison of numerical and experimental results for delamination front position (mm) with an applied bending moment of 60 Nm (step 4). In order to easy the reading and interpretation of the results, the X coordinate at which the crack front is located is marked with an arrow at selected points.**

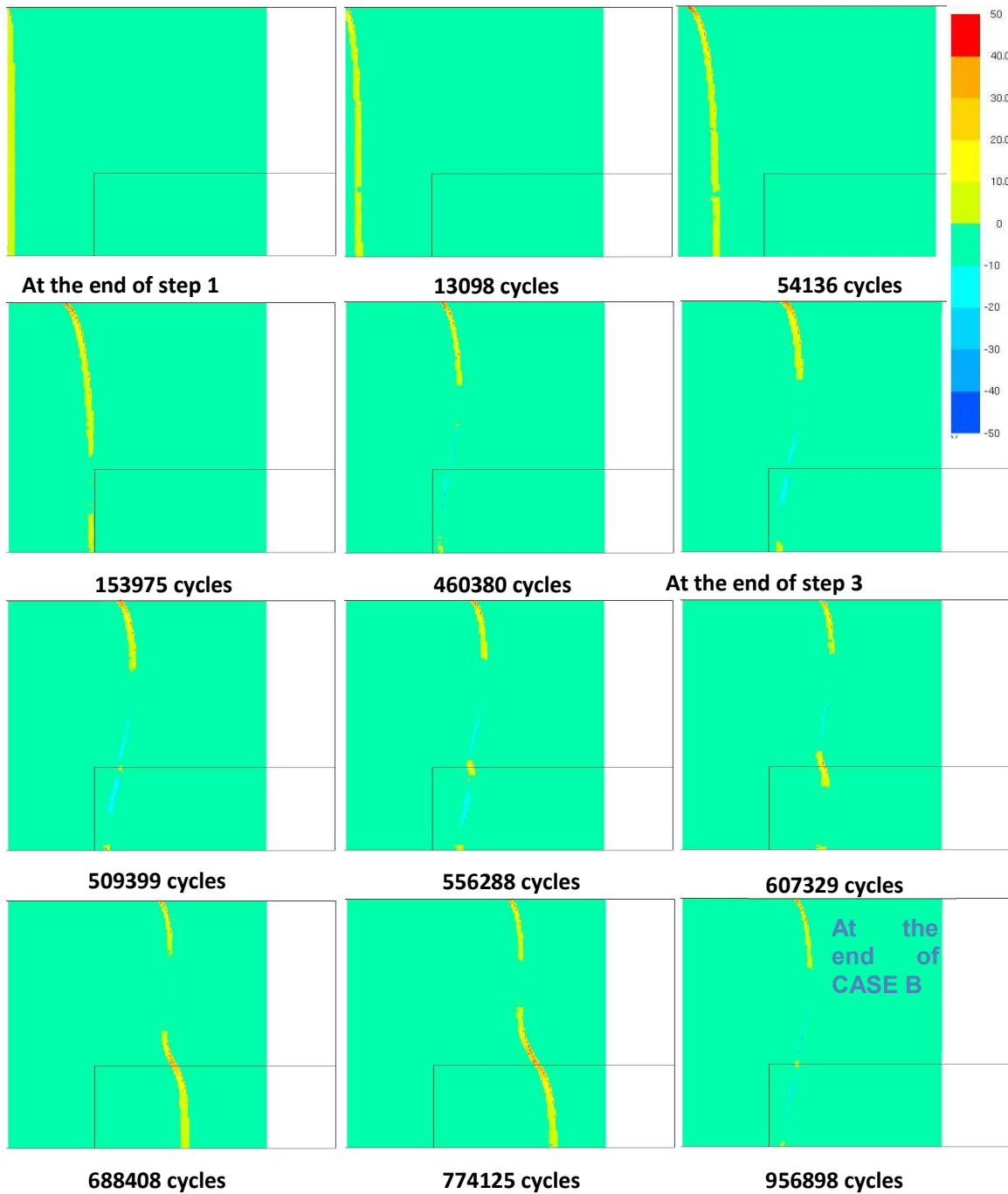
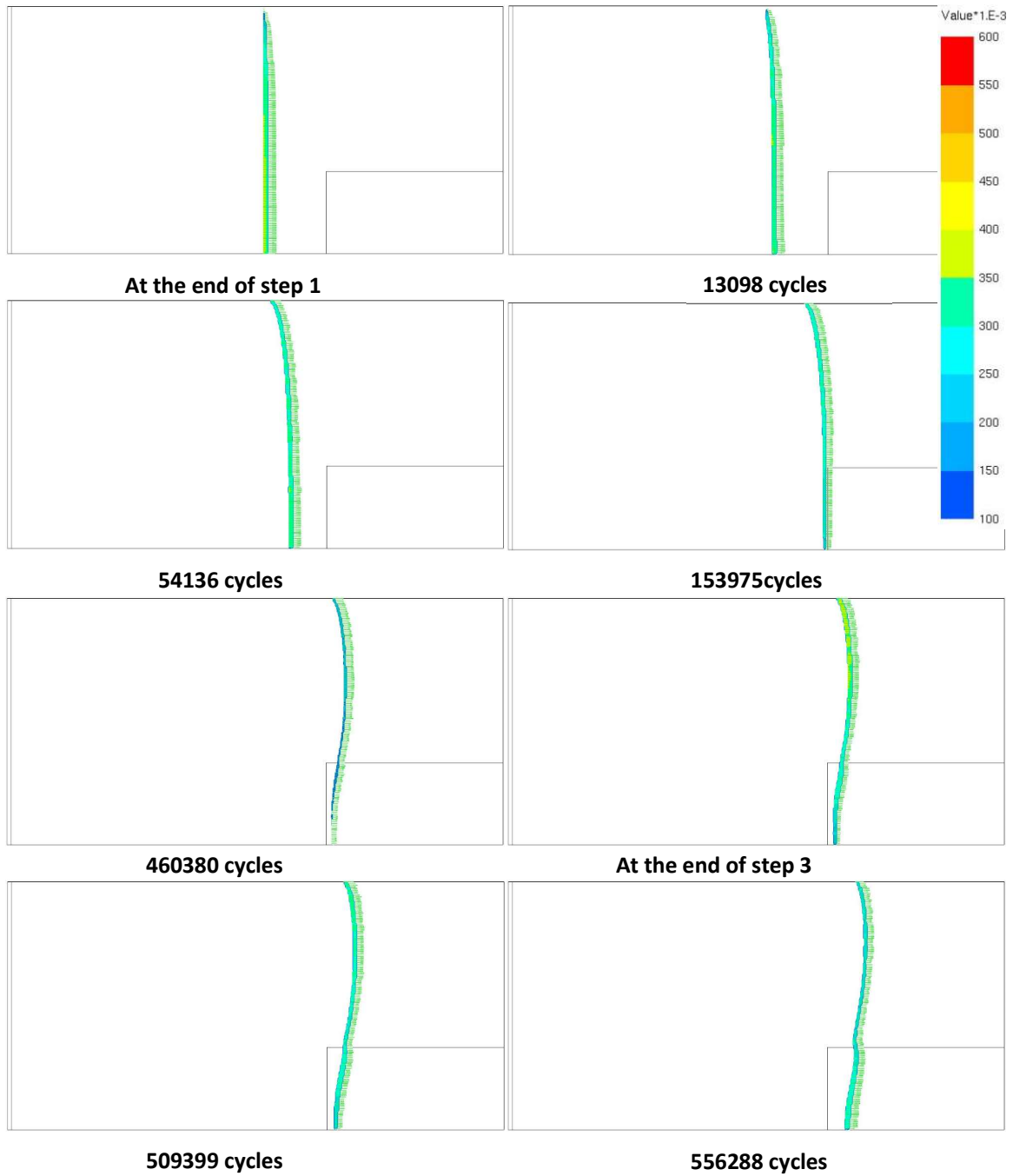


Figure 4-23: Evolution of GDD (in degrees) – steps from 1 to 4 of CASE A and at the end of CASE B





Continued on next page



**Figure 4-24: Evolution of mode I component of the J integral (N/mm) – steps from 1 to 4 of CASE A and at the end of CASE B.**

## 5. Conclusions

---

An interlaminar damage fatigue model was developed. The innovation, with respect to the current state-of-the-art, is that the model is ready for its use in the prediction of fatigue-driven delamination in 3D structures with accurate measurement of the energy release rate.

The interlaminar damage fatigue model, presented in Section 2 and published in a high quality international peer reviewed scientific journal<sup>1</sup> and an open access archive<sup>2</sup>, was implemented in Simcenter Samcef solver 1980 as a native behaviour. The implementation was validated by comparison of the results of several simple test cases with the initial development implementation by AAU in Abaqus as a user element.

In order to assess the prediction capabilities of the model, a demonstrator specimen showing changing crack front shape and propagation rate along the fatigue analysis was designed. A full characterization campaign on coupon test specimens was performed to obtain the properties that input the model. Then, the implementation in Samcef solver was used to perform the simulation of the demonstrator specimen test and the results were compared to the experimental results obtained at AAU lab facilities. The CPU time was reasonably low (6h 30 min with sequential execution, which might be improved by parallelization). This enables modelling, in subsequent WP5 tasks, a real wind turbine blade component substructure.

The shape of the crack propagation was well reproduced. The crack front propagation was slightly underestimated compared to the experimental results. The difference between experimental and simulation results at the end of the analysis is about is comparable to the variation in crack propagation among the different demonstrator specimens experimentally tested. Moreover, the significant variation between the different experimental set results used to characterize the material fatigue properties from coupon specimens, especially at low energy release rates, can explain the difference between numerical and experimental results on the demonstrator specimen.

The developed simulation tool has shown to be capable to estimate the evolution of interlaminar fatigue damage in a 3D analysis with high efficiency and reasonable accuracy.

## 6. References

---

1. Carreras, L. *et al.* A simulation method for fatigue-driven delamination in layered structures involving non-negligible fracture process zones and arbitrarily shaped crack fronts. *Compos. Part A Appl. Sci. Manuf.* **122**, 107–119 (2019).
2. Carreras, L. *et al.* A simulation method for fatigue-driven delamination in layered structures involving non-negligible fracture process zones and arbitrarily shaped crack fronts. *arXiv* <https://arxiv.org/abs/1905.05000> (2019).
3. Dugdale, D. S. Yielding of steel sheets containing slits. *J. Mech. Phys. Solids* **8**, 100–104 (1960).
4. Barenblatt, G. I. The mathematical theory of equilibrium cracks in brittle fracture. *Adv. Appl. Mech.* **7**, 55–129 (1962).
5. Bak, B. L. V., Turon, A., Lindgaard, E. & Lund, E. A simulation method for high-cycle fatigue-driven delamination using a cohesive zone model. *Int. J. Numer. Methods Eng.* **106**, 163–191 (2016).
6. Jensen, S. M., Martos, M. J., Lindgaard, E. & Bak, B. L. V. Inverse parameter identification of n-segmented multilinear cohesive laws using parametric finite element modeling. *Compos. Struct.* **225**, 111074 (2019).
7. Spearing, S. M. & Evans, A. G. The role of fiber bridging in the delamination resistance of fiber-reinforced composites. *Acta Metall. Mater.* **40**, 2191–2199 (1992).
8. Olsson, R., Thesken, J. C., Brandt, F., Jönsson, N. & Nilsson, S. Investigations of delamination criticality and the transferability of growth criteria. *Compos. Struct.* **36**, 221–247 (1996).
9. Lindgaard, E. & Bak, B. L. V. Experimental characterization of delamination in off-axis GFRP laminates during mode I loading. *Compos. Struct.* **220**, 953–960 (2019).
10. Carreras, L., Bak, B. L. V., Turon, A., Renart, J. & Lindgaard, E. Point-wise evaluation of the growth driving direction for arbitrarily shaped delamination fronts using cohesive elements. *Eur. J. Mech. A/Solids* **72**, 464–482 (2018).
11. Carreras, L., Lindgaard, E., Renart, J., Bak, B. L. V. & Turon, A. An evaluation of mode-decomposed energy release rates for arbitrarily shaped delamination fronts using cohesive elements. *Comput. Methods Appl. Mech. Eng.* **347**, 218–237 (2019).
12. Benzeggagh, M. L. & Kenane, M. Measurement of mixed-mode delamination fracture toughness of unidirectional glass/epoxy composites with mixed-mode bending apparatus. *Compos. Sci. Technol.* **56**, 439–449 (1996).
13. Turon, A., Camanho, P. P., Costa, J. & Dávila, C. G. A damage model for the simulation of delamination in advanced composites under variable-mode loading. *Mech. Mater.* **38**, 1072–1089 (2006).
14. Turon, A., González, E. V., Sarrado, C., Guillaumet, G. & Maimí, P. Accurate simulation of delamination under mixed-mode loading using a cohesive model with a mode-dependent penalty stiffness. *Compos. Struct.* **184**, 506–511 (2018).
15. Sarrado, C., Turon, A., Renart, J. & Urresti, I. Assessment of energy dissipation during mixed-mode delamination growth using cohesive zone models. *Compos. Part A Appl. Sci. Manuf.* **43**, 2128–2136 (2012).
16. Downing, S. D. & Socie, D. F. Simple rainflow counting algorithms. *Int. J. Fatigue* **4**, 31–40 (1982).
17. Marsh, G. *et al.* Review and application of Rainflow residue processing techniques for accurate fatigue damage estimation. *Int. J. Fatigue* **82**, 757–765 (2016).
18. Paris, P. & Erdogan, F. A critical analysis of crack propagation laws. (1963).

19. Blanco, N., Gamstedt, E. K., Asp, L. E. & Costa, J. Mixed-mode delamination growth in carbon–fibre composite laminates under cyclic loading. *Int. J. Solids Struct.* **41**, 4219–4235 (2004).
20. Sørensen, B. F., Jørgensen, K., Jacobsen, T. K. & Østergaard, R. C. DCB-specimen loaded with uneven bending moments. *Int. J. Fract.* **141**, 163–176 (2006).
21. Hutchinson, J. W. & Suo, Z. Mixed mode cracking in layered materials. in *Advances in applied mechanics* **29**, 63–191 (Elsevier, 1991).
22. Dessureautt, M. & Spelt, J. K. Observations of fatigue crack initiation and propagation in an epoxy adhesive. *Int. J. Adhes. Adhes.* **17**, 183–195 (1997).
23. Bak, B. L. V. & Lindgaard, E. A method for automated digital image-based tracking of delamination fronts in translucent glass fibre-laminated composite materials. *Strain* e12345 (2020).
24. Lloyd, S. Least squares quantization in PCM. *IEEE Trans. Inf. theory* **28**, 129–137 (1982).
25. MathWorks Inc., T. Filtering and Smoothing Data. Available at: <https://se.mathworks.com/help/curvefit/smoothing-data.html>.
26. Carreras, L., Bak, B. L. V., Turon, A., Renart, J. & Lindgaard, E. Point-wise evaluation of the growth driving direction for arbitrarily shaped delamination fronts using cohesive elements. *Eur. J. Mech. - A/Solids* **72**, 464–482 (2018).